








Late Cambrian Syn-Intrusive Thickening of the Ikh Mongol Arc Domains in the Mongolian Collage



Key Points:

- 500–490 Ma syn-intrusive lateral shortening of the Ikh Mongol Arc domain
- Cooling history is compatible with shortening and/or erosion of hot crust
- 500 Ma granulite-migmatite zone flanks Precambrian microcontinents of the Central Asian Orogenic Belt

Vít Peřestý¹ , Igor Soejono¹, Karel Schulmann^{1,2}, Gilles Ruffet³ , Andrew Kylander-Clark⁴ , Jiří Sláma⁵ , Pavla Štípská¹ , Petra Maierová¹ , Pavel Hanžl¹, Carmen Aguilar⁶ , and Adam Kašpar⁷

¹Czech Geological Survey, Prague, Czech Republic, ²Université de Strasbourg, CNRS, IPGS UMR 7516, Strasbourg, France, ³CNRS, Université Rennes, Géosciences Rennes - UMR 6118, Rennes, France, ⁴Department of Earth Science, University of California, Santa Barbara, CA, USA, ⁵Institute of Geology of the Czech Academy of Sciences, Prague, Czech Republic, ⁶Departament de Mineralogia, Petrologia i Geologia Aplicada, Facultat de Ciències de la Terra, Universitat de Barcelona, Zona Universitària de Pedralbes, Barcelona, Spain, ⁷Independent Researcher, Hanušovice, Czech Republic

Supporting Information:

Supporting Information may be found in the online version of this article.

Correspondence to:

V. Peřestý,
vit.peresty@geology.cz

Citation:

Peřestý, V., Soejono, I., Schulmann, K., Ruffet, G., Kylander-Clark, A., Sláma, J., et al. (2025). Late Cambrian syn-intrusive thickening of the Ikh Mongol Arc domains in the Mongolian Collage. *Tectonics*, 44, e2024TC008437. <https://doi.org/10.1029/2024TC008437>

Received 10 JUN 2024
Accepted 4 DEC 2024

Abstract Structural analysis, U–Pb monazite and xenotime dating, Ar–Ar dating of biotite and amphibole and thermodynamic modeling of peak metamorphic assemblages allow constraining the tectono-thermal evolution of the migmatite-magmatite domain on the southern periphery of Precambrian Zavkhan Block. The main subvertical metamorphic fabric resulted from upright folding and almost complete transposition of early sub-horizontal foliation of uncertain age. P–T conditions of 760–790°C at 0.7–0.8 GPa and in situ U–Pb metamorphic monazite 505–495 Ma ages characterize this tectono-metamorphic event. It was associated with syn-deformational partial melting and intrusion of axial planar syntectonic leucogranite veins. Monazite and xenotime from these veins give U–Pb age of c. 500 Ma, confirming that the migmatization and formation of subvertical fabric were coeval. Such time constraints are contemporaneous with ages of gneissified Ikh-Mongol Arc granite sheets intruding horizontally shortened partially molten crust thereby confirming syn-compressional nature of arc emplacement. Thermal modeling of cooling history of the whole migmatite-magmatite domain constrained by Ar–Ar ages is compatible with the shortening of the hot system followed by moderate erosion. The P–T and geochronological data of the Zavkhan block margin are almost identical to those of short lived late Cambrian magmatism and metamorphism described in the Khondalite belt in Far East China and in other places of Mongolian Collage suggesting that these two domains may have formed a continuous belt.

1. Introduction

Magmatic arcs play an important role in the accretionary history of the Altaides (Şengör et al., 1993) known also as Central Asian Orogenic Belt (CAOB; Mossakovsky et al., 1993), which represents one of the world's largest Phanerozoic accretionary orogens. This large orogenic system interpreted as supercollage by Xiao et al. (2015), may be divided into three “collages” that each experienced a different accretionary history: (a) the western Kazakhstan Collage, (b) the eastern Mongolian Collage and (c) the southern Tarim-North China Collage (Figure 1b). The first two collages were affected by seaward migration of magmatic arcs from the Cambrian to Carboniferous (e.g., Sengör & Natal'in, 1996). The migration of these arcs over the accretionary complexes was interpreted to be related to the roll-back of the enigmatic Paleo-Asian Ocean (e.g., Xiao et al., 2018), but recent investigations show that at least for the Mongolian Collage, the ocean involved for the early Paleozoic period was Panthalassa (Paleo-Pacific; Jiang et al., 2017). Although most of the magmatic arcs are oceanic and poorly preserved (Safonova et al., 2017), there is one giant Japan-type magmatic arc firmly established on the western and southern “external” margins of the Precambrian continental crust of the Mongolian Collage, the c. 1,800 km long Cambrian–Ordovician Ikh Mongol Arc (Figure 1b; Janoušek et al., 2018).

Although, the chemistry and timing of Cambrian–Ordovician magmatism were extensively studied by many authors (e.g., Rudnev et al., 2009, 2013; Salnikova et al., 2001; Soejono et al., 2016; Yarmolyuk et al., 2011) the tectonic regime controlling the emplacement mode of magmatic bodies was so far not addressed. It is generally accepted, that this arc formed above a retreating subduction system and its at least 60-Myr-long life span was intimately connected to the sedimentary infill of a contemporaneous accretionary wedge (e.g., Chen et al., 2015; Hanžl et al., 2024; Jiang et al., 2011, 2017; Long et al., 2007; Soejono et al., 2018). Altogether, it was tacitly assumed that the long-lasting rollback of the oceanic plate generated a magmatic arc together with a giant accretionary forearc basin during a long-lasting extensional regime (e.g., Buriánek et al., 2022).

© 2024. The Author(s).

This is an open access article under the terms of the [Creative Commons Attribution License](https://creativecommons.org/licenses/by/4.0/), which permits use, distribution and reproduction in any medium, provided the original work is properly cited.

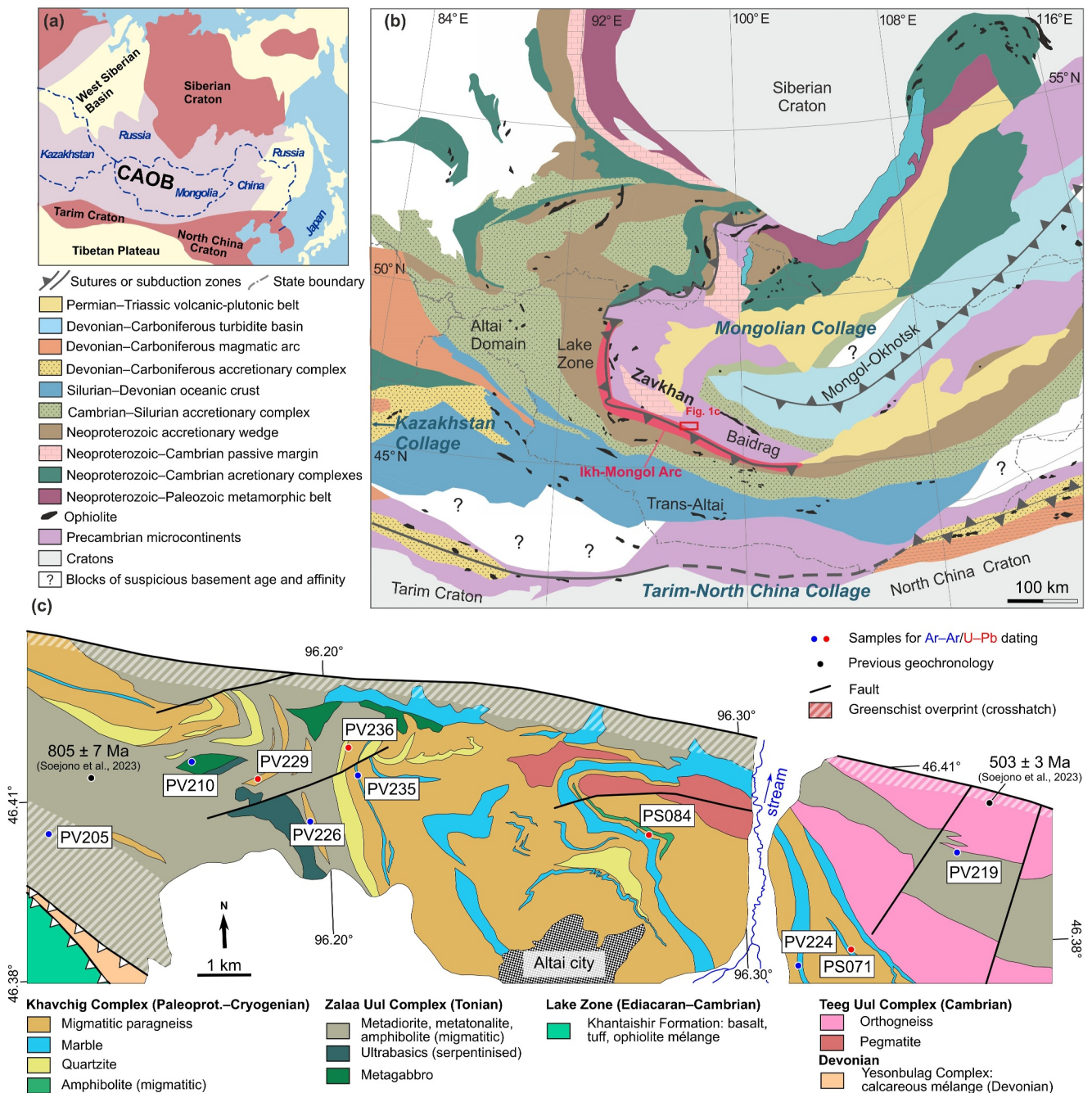


Figure 1. Central Altai Orogenic Belt (CAOB) and study area. (a) Position of the CAOB after Şengör et al. (1993). (b) Internal zoning of the CAOB after Soejono et al. (2021). (c) Geological map of studied area highlighted in (b) based on new mapping and Togtokh et al. (1995).

This study attempts to characterize the tectonic regime of Ikh Mongol Arc emplacement and to relate it to the general geodynamic scenario of the formation of the Mongolian Collage. We propose that the studied migmatitic-magmatic domain on the margin of the Zavkhan Block belongs to deep crustal levels of the Ikh Mongol Arc edifice. We present new U–Pb monazite and xenotime ages of metasediments and their partial melts, $^{40}\text{Ar}/^{39}\text{Ar}$ amphibole and biotite ages, structural data and estimates of peak P–T conditions. These new data show that at the Cambrian–Ordovician boundary, the high-temperature metamorphism occurred synchronously with the main period of Ikh Mongol Arc magmatism. The structural record indicates that the arc magmas were emplaced as vertical sheets parallel to the vertical anisotropy of hot host-rocks during the late Cambrian contractional regime.

Similarities with the NE China Khondalite Belt in the east and differences with the Sayan-Baikal orogen in the north allow proposing a new model of early Paleozoic construction of the Mongolian Collage.

2. Geological Setting

2.1. Regional Background

The Mongolian segment of the CAOBS occupies territory between the Siberian Craton to the north and the Tarim and North China cratons to the south (Figure 1a). The Mongolian Collage (Xiao et al., 2015) at the eastern part of the CAOBS resulted from successive accretion of micro-continental blocks, ophiolites, magmatic arcs, accretionary wedges and back-arc basins to the southern margin of Siberia (e.g., Badarch et al., 2002; Kröner et al., 2014; Safonova et al., 2017).

It has been shown that the complex geological architecture of the Mongolian Collage originates from the long-lasting Neoproterozoic to Permian–Triassic multi-stage evolution (e.g., Wilhem et al., 2012; Windley et al., 2007; Xiao et al., 2015) including: (a) the Tonian active margin of Rodinia followed by development of passive margin sequences associated to its break-up and drift of the individual micro-continental blocks away from the Rodinian margin (Kovach et al., 2021; Kozakov et al., 2014; Levashova et al., 2010; Soejono et al., 2023; Štípská et al., 2023), (b) late Ediacaran to early Cambrian closure of multiple oceanic basins between these micro-continents and Siberia (Buriánek et al., 2017; Donskaya et al., 2017; Gladkochub et al., 2008; Sukhbaatar et al., 2024; Štípská et al., 2024), (c) early Paleozoic active margin related to the subduction of the Paleo-Pacific oceanic plate beneath the Mongolian Collage micro-continental ribbon (Janoušek et al., 2018; Jiang et al., 2017; Kröner et al., 2010; Soejono et al., 2021; Xiao et al., 2004) and finally (d) the late Paleozoic–Mesozoic collisional evolution (Aguilar et al., 2024; Guy et al., 2014; Xiao et al., 2018).

This study focuses on the southern edge of the Zavkhan Block, one of the major fragments of Precambrian crust in the Mongolian Collage (Figure 1). The Zavkhan Block consists of the Archean to Mesoproterozoic basement (Dergunov et al., 1997; Kozakov et al., 2007; Mitrofanov et al., 1985) and its Neoproterozoic to Lower Cambrian passive margin sequences (Bold et al., 2016; Kovach et al., 2021; Kozakov et al., 2014; Levashova et al., 2010). The Lake Zone contains the Neoproterozoic ophiolites, accretionary wedges and oceanic arcs accreted against or thrust over the northerly basement of the Zavkhan Block during the early Cambrian (Skuzovatov et al., 2018; Štípská et al., 2010). Both the continental basement and the Lake Zone were intruded by the Cambrian–Ordovician (c. 530–470 Ma) arc-type rocks (Dijkstra et al., 2006; Kovach et al., 2011; Marinov et al., 1973) of the Ikh Mongol Arc (Janoušek et al., 2018). South of the Lake Zone is an up to 300-km-wide late Cambrian to Silurian volcanic-sedimentary complex of the Mongol Altai Zone, recently interpreted as a giant accretionary wedge sourced from the northerly Ikh Mongol Arc (Jiang et al., 2017; Soejono et al., 2018; Xiao et al., 2009). This complex was metamorphosed, intruded by large quantities of Devonian granitoids and unconformably covered by Devonian extensional sedimentary basins (e.g., Buriánek et al., 2022; Jiang et al., 2016).

2.2. Geology of the Studied Area

The study area is situated on the southern periphery of the Zavkhan Block, close to the contact with the Lake Zone, in the vicinity of Altai City (Figure 1c). Based on the lithology, age and structural record, the rocks of interest can be subdivided into three lithotectonic units (Bold et al., 2016; Soejono et al., 2023; Togtokh et al., 1995): the (a) metasedimentary Khavchig Complex and the (b) metaigneous Zala Uul Complex which are both intruded by the (c) metaigneous Teeg Uul Complex. The rocks of these three units are interfolded together and separated from the southwestern Lake Zone by thrust faults (Figure 1c).

The rock assemblage of the Khavchig Complex consists of alternating biotite paragneiss, sometimes with garnet and/or sillimanite (Figure 2d), coarse-grained marble (up to c. 1 cm grain size), quartzite, migmatitic amphibolite (\pm garnet) and calc-silicate. The whole sequence is intruded by coarse-grained pegmatite (with up to decimeter scale feldspars), that are preferentially associated with marble or quartzite bodies. The U–Pb dating of detrital zircons (Bold et al., 2016; Soejono et al., 2025) showed both the Paleoproterozoic and Neoproterozoic maximum depositional ages of the Khavchig Complex metasediments, indicating transgressive relationship or tectonic juxtaposition of stratigraphically distinct sequences.

The Zala Uul Complex is a high-grade metamorphic unit, whose protoliths are mainly intermediate to mafic magmatic rocks (granodiorite, tonalite and gabbro) transformed into orthogneiss, amphibolite, metagabbro and

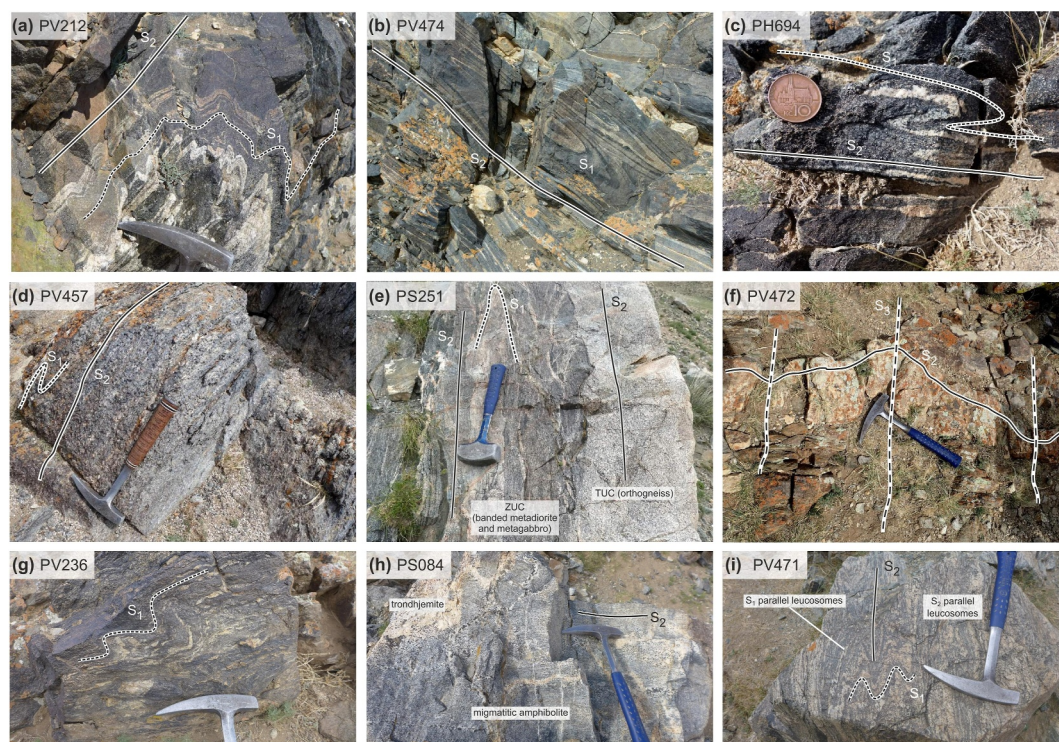


Figure 2. Field photographs. (a) Hinge zone of folded S_1 fabric in banded amphibolite of Zala Uul Complex. (b) Domain of tight to isoclinal F_2 folds in banded amphibolite (Zala Uul Complex). (c) Asymmetric F_2 fold in migmatitic amphibolite (Zala Uul Complex, map view). (d) Main S_2 fabric in sillimanite-garnet gneiss (Khavchig Complex). (e) Intrusive contact of Teeg Uul orthogneiss with Zala Uul migmatitic amphibolite—note complex structural record and higher strain in the amphibolite contrasting to simple S_2 fabric in the orthogneiss. (f) Open F_3 folds with weakly developed S_3 fracture cleavage in pegmatite dike parallel to S_2 (Khavchig Complex, map view). (g) Migmatitic fabric in the gneiss of the Khavchig Complex. (h) Migmatization in amphibolites (Khavchig Complex). (i) S_1 and S_2 parallel leucosomes in gneiss (Khavchig Complex).

amphibole-biotite gneiss (Figures 2a–2c, Soejono et al., 2023). Recent U–Pb zircon dating of the Zala Uul Complex (orthogneiss, metatonalite) by Soejono et al. (2023) yielded Tonian ages (830–805 Ma), which have been interpreted as the timing of magma crystallization in an extensional setting. Serpentinized ultramafic bodies are usually spatially linked to coarse-grained gabbroic intrusions. Most of the rock types show evidence for partial melting, as documented by numerous, mainly trondhjemitic centimeter- to meter-scale dikes and melt-pods (usually folded, Figures 2a and 2c).

In contrast to the Zala Uul Complex, the Teeg Uul Complex is characterized by lithologically rather homogeneous medium-grained equigranular felsic orthogneiss with biotite and amphibole, dated by Soejono et al. (2023) to 503 ± 3 Ma. The orthogneiss shows intrusive relationships to the host Zala Uul Complex (Figure 2e) as well as to the Khavchig Complex.

As described above, the majority of the rocks in the Zala Uul and Khavchig complexes show evidence of partial melting. However, the westernmost part of the Zala Uul Complex close to the contact with the Lake Zone and most of the complexes along the contact with the northern limiting fault are affected by a low-grade greenschist-facies overprint (Figure 1c).

3. Structural Record

The structural record in the area results from the superposition of four distinct deformation events (D_1 – D_4), which together led to a complex fold interference pattern in the map view (Figure 3a). The oldest metamorphic foliation S_1 appears locally as relics folded by cm-scale close to isoclinal folds F_2 with variable, but usually steep fold axes L_2 (Figures 2a–2c and 3b). Importantly, such folds have not been observed in the Teeg Uul Complex, where S_1 is

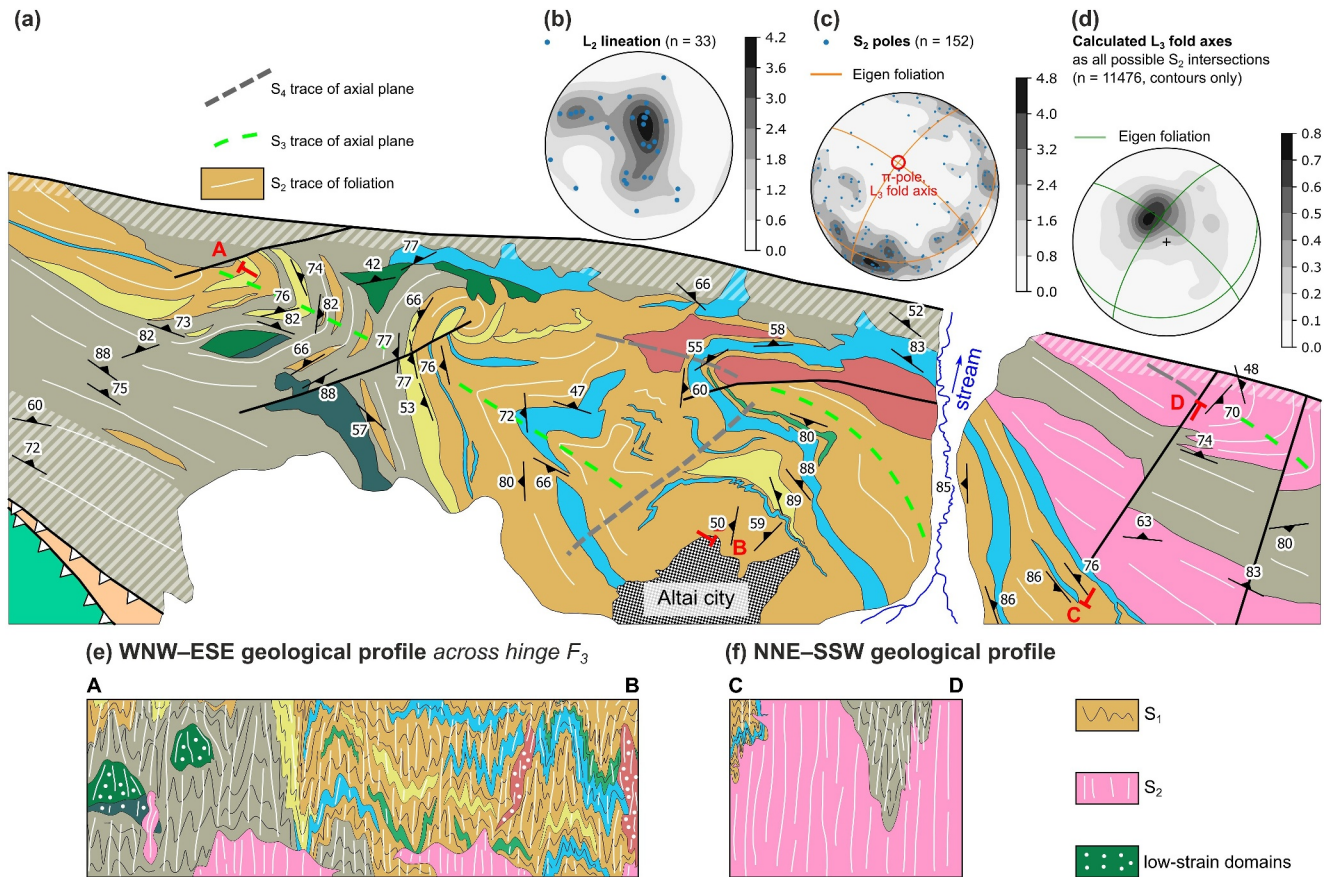


Figure 3. Structural record. (a) Structural map of the area, for lithological legend see Figure 1c. (b) Fold axes and intersection lineation L_2 . (c) Poles to the main S_2 fabric, eigen foliations of the orientation tensor are shown, together with the corresponding π -pole. (d) L_3 fold axes are represented as a contoured set of S_2 self-intersections, compatible with the π -pole in (c).

apparently missing (see also Soejono et al., 2023). S_1 is in most places completely transposed by the dominant, subvertical fabric S_2 developed in all the complexes. The S_2 is commonly a migmatitic fabric, defined by alternating melanosome and lecosome bands (Figure 2). In stereonet, the poles to the S_2 foliation are distributed along a fully developed girdle with subvertical NNE-dipping maximum and steep, north-dipping π -pole (Figure 3c). The formation of the girdle results from the superposed, post-metamorphic event D_3 , responsible for a large-scale folding in the map view and small-scale heterogeneously developed open folds and crenulations with subvertical L_3 fold axes (Figure 3c). The fold axes of large-scale folds are equivalent to the orientation of the π -pole of the S_2 girdle in Figure 3c, whose orientation is compatible with the fold axes calculated as all possible intersections of the S_2 limbs (Figure 3d). There is usually no new S_3 fabric related to the D_3 event, apart from rarely developed subvertical NW–SE to NS trending fracture cleavage (Figure 2f). Similarly, the post-metamorphic event D_4 weakly modified the existing pattern by large-scale open folds F_4 with subvertical NE-trending axial planes (Figure 3a) resulting in the final map-view fold interference pattern (with shared fold axis, type 3 of Ramsay, 1967).

This work focuses on the tectonic significance of the main S_2 fabric, whose relationships to the migmatitic event D_2 – M_2 can be best illustrated on the key outcrop PV229 (Figure 4). The outcrop is dominated by banded amphibole-biotite gneiss and leucogranite dikes (Figures 4b and 4d). Amphibolite and calc-silicate are less frequent and occur as boudins within the host gneiss (Figures 4a and 4c). The main foliation S_2 is steeply NW to NNW dipping and originates as an axial-planar cleavage of widespread closed to isoclinal F_2 folds (Figures 4b–4d), with fold axes plunging steeply to the N. The relationship of the leucosomes to the main S_2 fabric is variable. Some leucosomes are cm-thick bands, sometimes with diffuse boundaries that are parallel to the strongly folded

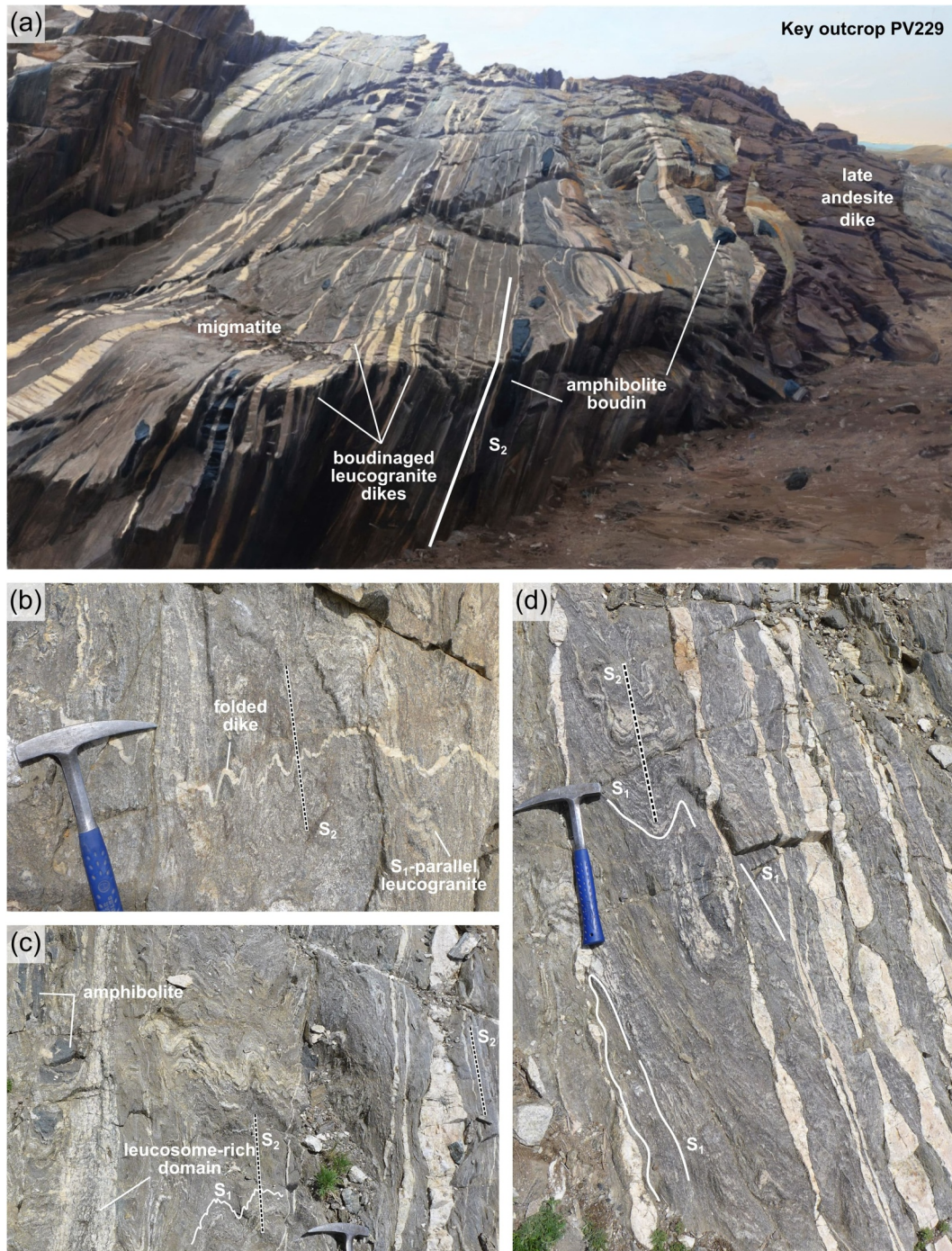


Figure 4. Key outcrop PV229 (96.184029°E, 46.411968°N). (a) Modified paint: Altai migmatites, oil on canvas, 110 × 180 cm, Adam Kašpar (2020, <https://www.adamkaspar.cz/en/>). (b) Folded leucogranite dike whose axial plane S_2 is parallel to the S_2 fabric in the host gneiss. (c) Competent amphibolite forms boudins in a relatively weak migmatitic gneiss, products of melting occur parallel to S_2 fabric (left), follow folded S_1 fabric (middle) or are boudinaged dikes (right). (d) Detail of boudinage of leucogranite dikes near parallel to S_2 fabric, which is axial planar to folded S_1 layering.

S_1 foliation. The proportion of leucosomes is variable and commonly follows the S_1 compositional banding, illustrating composition-dependent productivity of melt during the D_2 - M_2 migmatization (Figures 4c and 4d). Another type is cm to several dm thick dikes affected by open-to-closed F2 folds (Figure 4b). Finally, some dikes are near-parallel to the main foliation S_2 and are commonly boudinaged (Figures 4a and 4d).

Table 1
Mineral Assemblages of Samples Selected for Ar–Ar Dating

| | PV210 | PV205 | PV219 | PV226 | PV224 | PV235 |
|---------------|------------|-------------|-------------|---------|-------------|--------|
| | Metagabbro | Amphibolite | Amphibolite | Gneiss | Amphibolite | Gneiss |
| | ZUC | ZUC | ZUC | KC | KC | KC |
| Dated phase | Amp | Amp | Amp | Amp, Bt | Amp | Bt |
| Quartz | | | x | x | | x |
| Plagioclase | x | x | x | x | x | x |
| Biotite | | | | x | | x |
| Sillimanite | | | | | | x |
| Amphibole | x | x | x | x | x | |
| Pyroxene | | | x | | x | |
| Chlorite | | x | | | | x |
| Sphene | | x | | | | |
| Retrogression | no | yes | no | no | no | yes |

Note. Symbol x marks presence of the mineral in the rock assemblage. ZUC—Zalaa Uul Complex, KC—Khavchig Complex.

4. Petrography

4.1. Approach and Methods

In order to characterize the prevalent migmatitic domain, we first provide a detailed description of three representative samples from the Khavchig Complex (PV236C, PS071F, and PS084E), including the chemistry of major rock-forming minerals. These samples have been used for in situ U–Pb dating and also for P–T modeling. For samples used for $^{40}\text{Ar}/^{39}\text{Ar}$ dating, we present only a description of mineral assemblages (Table 1), as the thin sections have not been investigated for mineral chemistry. For detailed methodology on data acquisition and processing see Supporting Information S1. Representative mineral analyses are in Table S1.

The sample PV236C is from the western part of the Khavchig Complex. It is a banded migmatite from an outcrop of alternating garnet-biotite migmatitic gneisses (locally with amphibole), garnetiferous quartzites and amphibolites. Sample PS071F is from the eastern part of the Khavchig Complex. It is an intercalation of migmatitic paragneiss in between coarse-grained marbles and quartzites. The selected sample PS084E is from the central part of the Khavchig Complex, from a complex outcrop with alternating migmatitic amphibolites (Figure 2h), marbles and selected coarse-grained garnetiferous paragneiss interpreted as melanosome-dominated rock.

4.2. Petrography of Modeled Samples

Paragneiss PV236C is a medium-grained, equigranular rock with a mineral assemblage garnet–biotite–K-feldspar–plagioclase–quartz–ilmenite (Figures 5a and 5b). Alignment of biotite flakes and aggregates ($x\text{Mg} = 42\text{--}44$, $\text{Ti} = 0.23\text{--}0.26$ a.p.f.u.) together with aggregate preferred orientation of plagioclase ($\text{Ab} = 76\text{--}80$, $\text{An} = 20\text{--}24$, $\text{Or} = 1$), K-feldspar ($\text{Or} = 80\text{--}92$, $\text{Ab} = 8\text{--}20$, $\text{An} = 0$) and quartz define the dominant S_2 foliation (Figure 5a). Presence of K-feldspar and absence of primary muscovite supports migmatitic character of the rock. Garnet (up to 2 mm) is usually subhedral to anhedral and contains inclusions mostly of quartz, but sometimes also of biotite ($x\text{Mg} = 55\text{--}60$, $\text{Ti} = 0.21\text{--}0.24$ a.p.f.u.), plagioclase, K-feldspar ($\text{Or} = 82$, $\text{Ab} = 17$, $\text{An} = 1$), ilmenite and monazite (Figures 5a, 5b, and 6a). Garnet has a high pyrope content and shows weak zoning with rimward increase of almandine and spessartine, decrease of pyrope and $x\text{Mg}$ in the very rim and has near constant grossular ($\text{Alm} = 74\text{--}77$, $\text{Grs} = 4$, $\text{Prp} = 18\text{--}13$, $\text{Sps} = 4\text{--}6$, $x\text{Mg} = 20\text{--}14$; Figure 6a). Fractures in the garnet are commonly filled by almost pure K-feldspar ($\text{Or} = 95\text{--}97$, $\text{Ab} = 3\text{--}5$, $\text{An} = 0$; Figure 5b), that may be interpreted as melt percolation through garnet fractures. Accessory minerals are apatite, monazite, zircon and magnetite.

Sample PS071F is a medium- to coarse-grained garnetiferous sillimanite–biotite paragneiss (Figure 5d). The S_2 foliation is defined by alignment of biotite ($x\text{Mg} = 53\text{--}56$, $\text{Ti} = 0.24\text{--}0.28$ a.p.f.u.) and of sillimanite grains and aggregates (Figure 5b). In addition, the matrix contains plagioclase ($\text{Ab} = 78\text{--}80$, $\text{An} = 9\text{--}20$, $\text{Or} = 0\text{--}2$), K-feldspar ($\text{Or} = 80\text{--}98$, $\text{Ab} = 2\text{--}20$, $\text{An} = 0$) and quartz as major phases. Sillimanite in the matrix is commonly

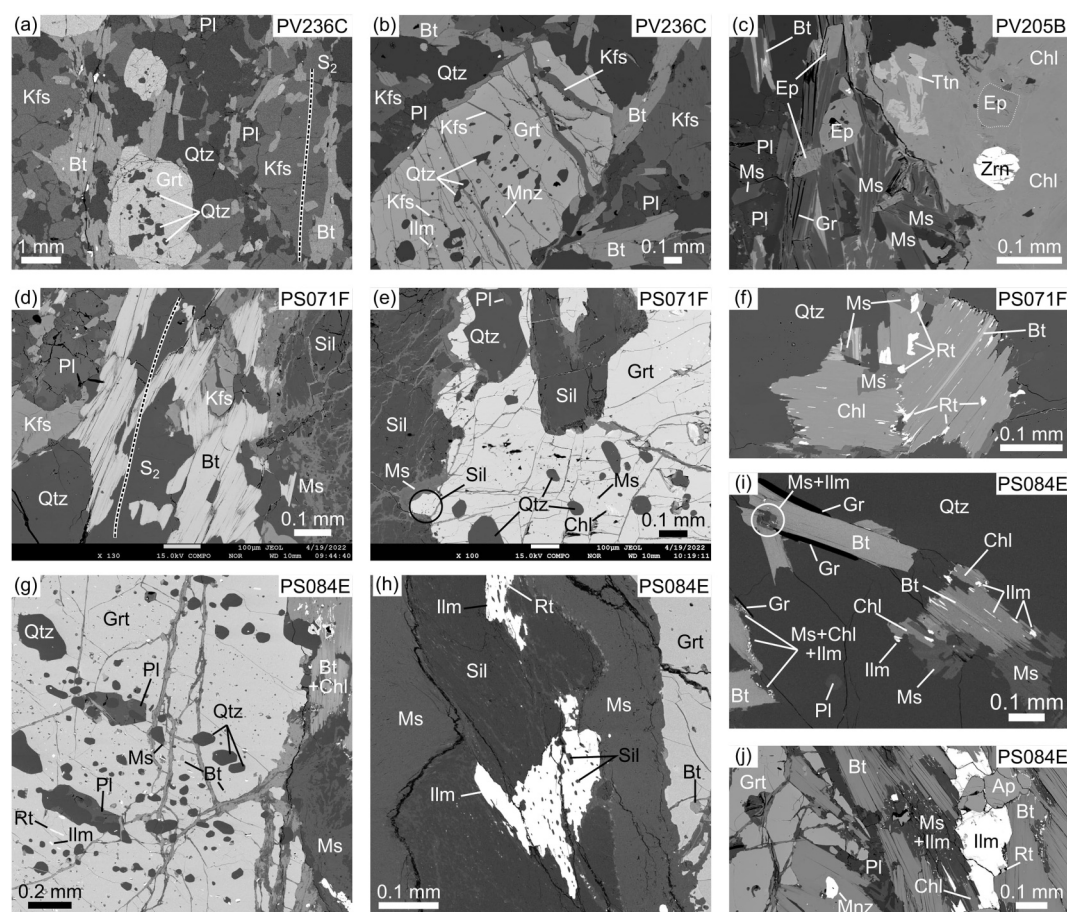


Figure 5. BSE images of selected samples. (a) S_2 foliation defined by alignment of biotite and aggregates of K-feldspar, plagioclase and quartz (PV236C). (b) Garnet porphyroblast with inclusions of quartz, ilmenite and monazite, note cracks filled by K-feldspar (PV236C). (c) Greenschist-facies assemblage (chlorite, epidote, muscovite, titanite) in a retrogressed gneiss in the vicinity of contact with Lake Zone (PV205B). (d) S_2 foliation bearing sillimanite, K-feldspar and biotite, sillimanite is replaced by muscovite along cracks (PS071F). (e) Zoom to garnet porphyroblast with inclusions of muscovite, chlorite and quartz and tiny sillimanite in the garnet rim, sillimanite surrounding garnet is replaced by muscovite (PS071F). (f) Chlorite-muscovite aggregate with relic biotite stripes and rutile formed probably during biotite breakdown (PS071F). (g) Typical inclusions in the rim of the garnet porphyroblast (PS084E). (h) Sillimanite is on the edge and along cracks replaced by muscovite and has ilmenite inclusions, ilmenite encloses sillimanite and relics of rutile (PS084E). (i)–(j) Products of biotite breakdown are chlorite, ilmenite and muscovite.

surrounded by fine-grained muscovite aggregates ($Si = 3.15\text{--}3.19$ a.p.f.u., $xNa = 2\text{--}3$, $xMg = 62\text{--}69$) and muscovite is present also in sillimanite cracks (Figures 5d and 5e). Additionally, muscovite ($Si = 3.18$ a.p.f.u., $xNa = 2$, $xMg = 59$) occurs in aggregates dominated by chlorite ($xMg = 53\text{--}54$, Figure 5f). Chlorite often surrounds biotite stripes and chlorite typically contains anhedral rutile inclusions sometimes aligned with its cleavage (Figure 5f). Anhedral porphyroblasts of garnet (up to 3 mm large, Figures 5e and 6b) are weakly zoned in the core, but has a strong retrograde zoning in the rim ($Alm = 62\text{--}68$, $Grs = 2\text{--}3$, $Prp = 29\text{--}18$, $Sps = 6\text{--}11$, $xMg = 31\text{--}20$, Figure 6b) and contains inclusions of quartz, muscovite ($Si = 3.14$ a.p.f.u., $xNa = 3$, $xMg = 36$), biotite, rutile, chlorite, monazite and in the rim inclusions of sillimanite (Figures 5e and 6b). Accessory minerals are apatite, graphite, rutile, monazite, xenotime and zircon. Migmatization in this sample is supported by the presence of K-feldspar and absence of primary muscovite.

Sample PS084E is a coarse-grained sillimanite–garnet–biotite paragneiss (Figures 5g–5j). The S_2 foliation is defined by the alignment of matrix biotite ($xMg = 34\text{--}37$, $Ti = 0.12\text{--}0.30$ a.p.f.u.) and sillimanite needles or aggregates. Major felsic minerals in the matrix are plagioclase ($Ab = 73\text{--}86$, $An = 14\text{--}26$, $Or = 0\text{--}1$) and quartz. Garnet porphyroblasts are up to 1 cm large, they are rich in inclusions and exhibit a strong zoning pattern ($Alm = 74\text{--}81$, $Grs = 12\text{--}4$, $Prp = 12\text{--}19\text{--}18$, $Sps = 2\text{--}1\text{--}2$, $xMg = 14\text{--}21\text{--}14$, Figure 6c). Garnet

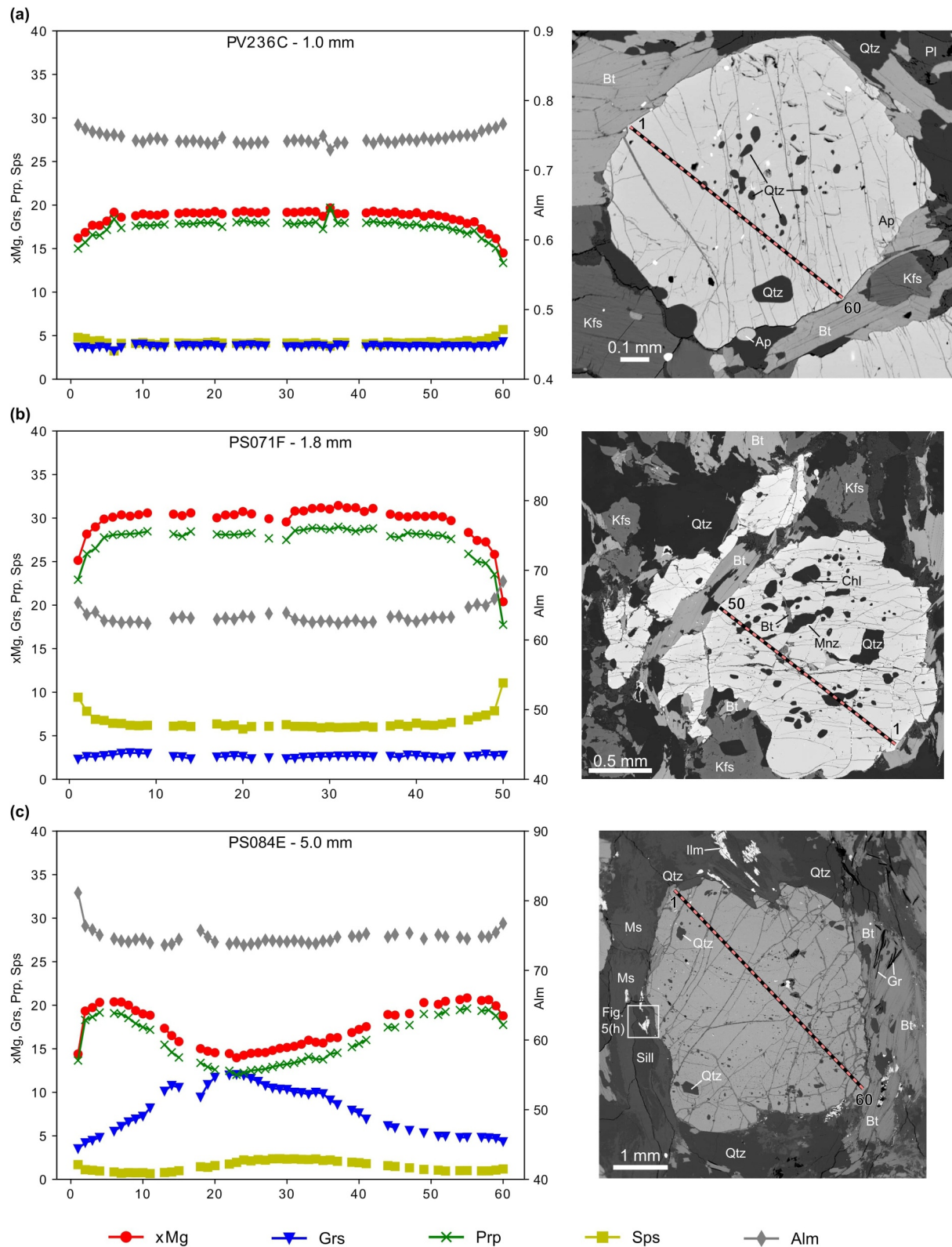


Figure 6. BSE images (right) of garnets and corresponding zoning profiles (left). Note graphite in BSE image in (c).

inclusions (Figure 5g) are quartz, biotite ($x\text{Mg} = 47\text{--}50$, $\text{Ti} = 0.21\text{--}0.30$ a.p.f.u.), plagioclase ($\text{Ab} = 67\text{--}87$, $\text{An} = 4\text{--}33$, $\text{Or} = 0\text{--}9$), muscovite ($\text{Si} = 3.03$ a.p.f.u., $x\text{Na} = 5$, $x\text{Mg} = 40$) and tiny chlorite ($x\text{Mg} = 34\text{--}51$). Rutile is enclosed preferentially in the garnet core, while sillimanite and ilmenite occur in the garnet rim. Muscovite ($\text{Si} = 2.99\text{--}3.11$ a.p.f.u., $x\text{Na} = 4\text{--}7$, $x\text{Mg} = 31\text{--}52$) is present also in the matrix as weakly oriented flakes or as fine-grained aggregates in between anhedral feldspars and as elongated aggregates surrounding sillimanite (Figure 5h). Muscovite and chlorite flakes are in the matrix spatially related to biotite (Figures 5i and 5j). Chlorite ($x\text{Mg} = 42$) typically contains ilmenite inclusions aligned parallel to the cleavage of chlorite. Ilmenite is in the matrix, but also as inclusions in sillimanite, where it contains euhedral sillimanite inclusions and tiny rutile anhedral pods (Figure 5h). The accessory phases are apatite, graphite, monazite and zircon.

5. P–T Modeling

Three samples have been modeled to obtain peak P–T conditions (PV236C, PS071F, and PS084E). All of the studied samples have migmatitic macroscopic features. We present results of garnet–sillimanite paragneiss PS071F and PS084E from the eastern and central part of the Khavchig Complex. Sillimanite-free sample PV236C is not shown, but gives overlapping P–T conditions.

For rocks formed at the P–T conditions above the wet solidus, the critical constraint affecting phase equilibria and the amount of melt is the water content. The calculations were done with c. 1 mol% of H_2O for PS071F and c. 2 mol% of H_2O for the sample PS084E, which allows stability of a very low amount of melt at calculated P–T conditions. Because even a small volume of melt escapes from the partially molten rock, such approach models the situation at peak temperature conditions, where rock is in equilibrium with small amount of generated melt (close to liquid-in line) and at the same time re-equilibration of a rock by hydration on a retrograde path is prevented. The prograde part of the rock evolution can not be constrained, because an unknown amount of melt has been lost and the bulk rock composition was therefore different. Some samples contain muscovite, rutile and chlorite inclusions in the garnet cores that may represent prograde stage, but large stability of these minerals in P–T space does not help to sufficiently constrain P–T conditions. Chlorite replacing matrix biotite and muscovite filling sillimanite cracks or replacing feldspars are considered as small-scale disequilibrium features related to hydration of the rock on a retrograde path whose P–T conditions can not be further constrained by pseudosection modeling (local equilibrium). Detailed methodology for phase equilibria modeling is provided in Supporting Information S1.

The peak assemblage Grt–Sil–Bt–Kfs–Pl–Rt–Qtz–L of the sample PS071F corresponds to the field at c. 760–800°C and 0.7–0.9 GPa, bounded by kyanite occurrence at higher pressure, ilmenite stability at lower pressure, absence of melt at lower temperature and breakdown of sillimanite at higher temperature (Figure 7a) and is compatible with garnet core composition ($x\text{Mg} = 29\text{--}31$, $\text{Gr}_s = 2\text{--}3$, $\text{Sp}_s = 6$, Figure 7b). Retrograde path marked by decreasing $x\text{Mg}$ and increasing Sp_s in the garnet rim is schematically shown by an arrow in Figures 7a and 7b.

For the sample PS084E, the peak assemblage Grt–Sil–Bt–Kfs–Pl–Ilm–Qtz–L corresponds to the field at c. 760–800°C and 0.5–0.8 GPa, bounded by rutile occurrence at higher pressure, cordierite stability at lower pressure, absence of melt at lower temperature and breakdown of biotite at higher temperature (Figure 7c). The composition of the garnet rim ($x\text{Mg} = 21$, $\text{Gr}_s = 4$, $\text{Sp}_s < 2$) with sillimanite and ilmenite inclusions is compatible with this field and grossular content favors rather its higher-pressure part (c. 0.7–0.8 GPa, Figure 7d). Decreasing $x\text{Mg}$ and on the edge of the garnet rim is schematically shown by an arrow in Figures 7c and 7d and is interpreted as retrograde re-equilibration of the grain. K-feldspar is minor in the sample, probably due to its later replacement by muscovite on a retrograde path.

6. U–Pb Monazite and Xenotime Dating

6.1. Methods

All monazite and xenotime grains have been analyzed in situ, using U–Pb ICP-MS dating. Samples PV236C, PS084E, and PS071F have been analyzed by Laser Ablation Split Stream (LASS) allowing simultaneous measurement of isotope ratios and element concentrations from the same volume of material. The LASS technique was not used for the sample PV229M; standard in situ dating was used instead. Detailed methodology is provided in Supporting Information S1 and analytical data in Table S2.

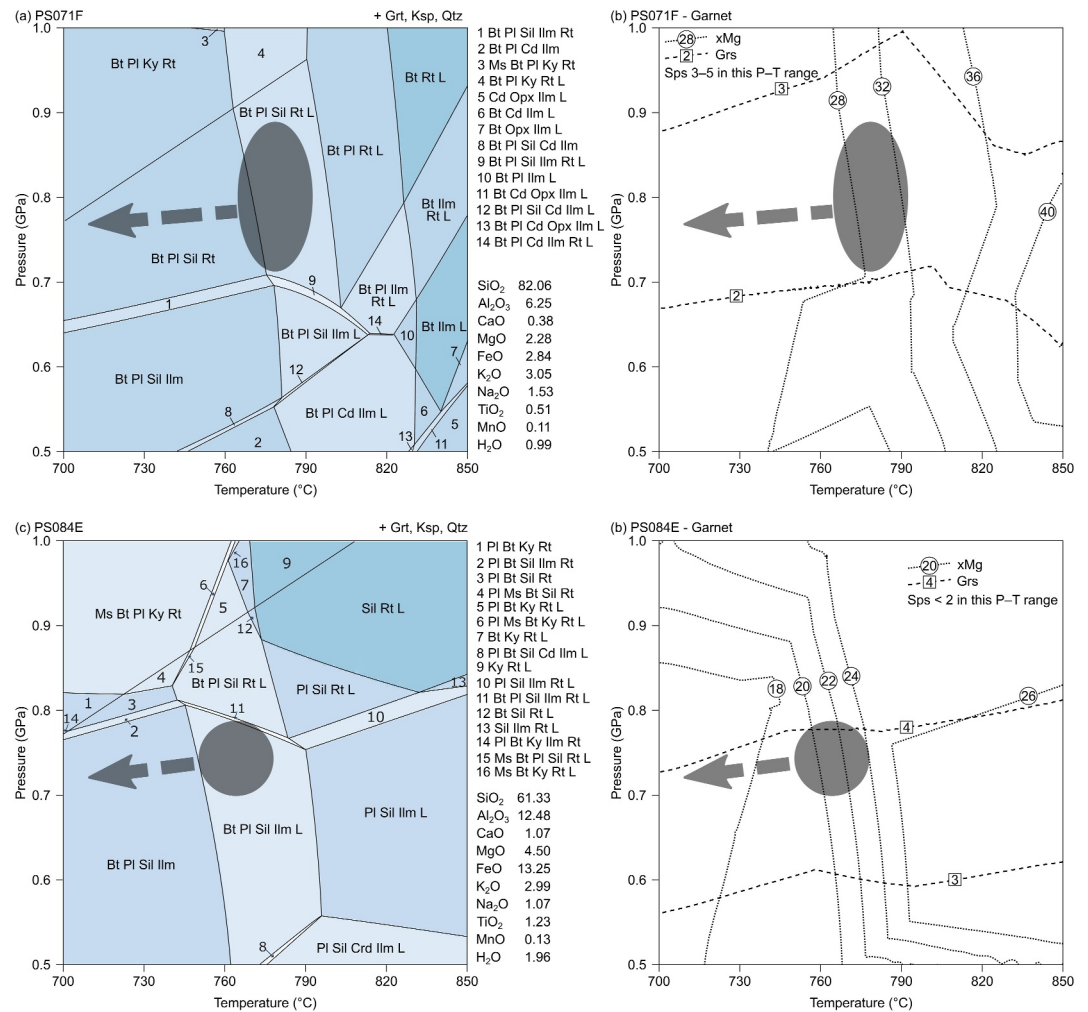


Figure 7. P–T pseudosections and garnet compositional isopleths of the sample PS071F (a, b) and PS084E (c, d). Inferred P–T conditions are highlighted by the ellipse. Bulk rock composition is in mol%. Melt is marked L.

6.2. Results of U–Pb Monazite and Xenotime Dating

Sample PV229M is from the key outcrop PV229. It is derived from a boudinaged leucogranite dike, subparallel to the S_2 fabric. The sample is composed of plagioclase, K-feldspar, quartz and accessory garnet, monazite and xenotime. Xenotime is euhedral to subhedral, up to 40 μm in size and shows oscillatory or sector zoning in BSE images (Figure 8a), monazite is subhedral to anhedral, up to 30 μm large and has sector or oscillatory zoning, but sometimes is structureless. Fourteen spots have been analyzed from five monazite grains, six of which gave a concordia age 497.2 ± 2.9 [5.8] Ma, which overlaps with intercept age 498.1 ± 2.5 [5.6] Ma (Figure 8a). Eleven spots have been measured in three xenotime grains, eight of which are concordant (502.2 ± 5.5 [7.4] Ma), overlapping within error with the intercept age 505.0 ± 5.4 [7.4] Ma for the whole group (Figure 8b).

In the sample PV236C (Figures 9a–9c, and 10a), 51 spots have been analyzed from 14 monazite grains located in the matrix or enclosed in the garnet. Monazite grains are rounded to subhedral, 20–40 μm large and weakly zoned with decreasing Y from the core to the rim (Figure 9a). There is no dependence of the age of the spots and the Y content (Figure 9b), but Y and HREE content correlate well with Eu (Figures 9a–9c and 10d). The grains in the garnet inclusions have rather high Eu, Y and HREE contents (Figures 9b, 9c, and 10d), but not a significant difference in age. The sample gives a single age group, with the lower intercept age of 502.0 ± 2.5 [5.6] Ma (Figure 10a). The discordant analyses are distributed along the corresponding Stacey–Kramers common lead trend and their intercept age overlaps with the age of concordant spots.

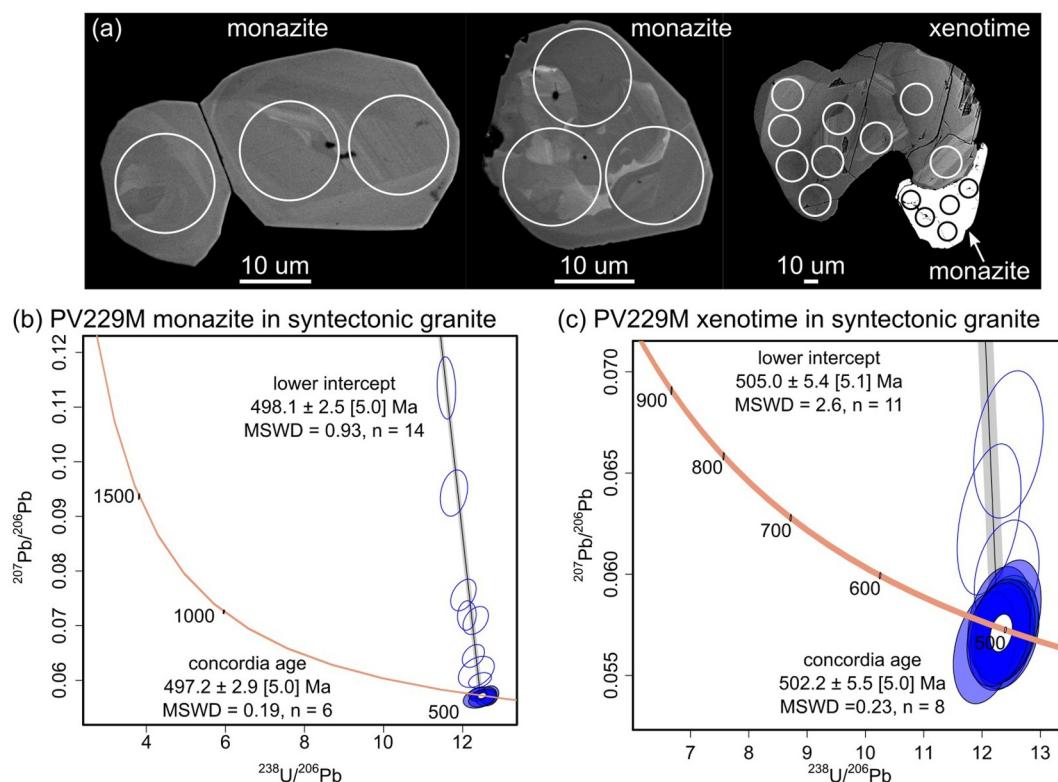


Figure 8. Monazite and xenotime in syntectonic leucogranite (sample PV229M). (a) Internal zoning in BSE. (b) Terra-Wasserburg concordia plot of analysed monazite spots. (c) Terra-Wasserburg concordia plot of analysed xenotime spots.

Monazites in the sample PS71F are located in the matrix or occur as garnet inclusions. They are subhedral to anhedral, rounded and up to 60 μm in size (Figure 9d). Internal structure characterized by Y-zoning is non systematic, generally demonstrating Y-rich cores, and Y-poor rims. Sometimes the cores show Y-rich annuli, while rims may have Y-rich apophyses (Figure 9d). There is no relation of age of the spot to the enclosing mineral (Figure 10d) nor in relation to Eu, Y or HREE content (Figures 9d–9f). Seventy-nine spots have been analyzed from 17 monazite grains, the discordant analyses are distributed along the corresponding Stacey-Kramers common lead trend and their intercept age overlaps with the age of concordant spots at $494.3 \pm 1.8 [5.3]$ (Figure 10b).

In the sample PS84E, 69 spots have been analyzed from 13 grains located in the matrix or enclosed by garnet and sillimanite (Figure 10d). The monazite crystals are usually rounded or with irregular grain boundaries, 20–80 μm large and have patchy Y-zoning (Figures 9g–9i). There is no correlation between the textural position of the monazite, its REE composition, Y content or age (Figures 9g–9i and 10d). The monazite ages define a single age group with the lower intercept age $503.3 \pm 1.7 [5.3]$ Ma (Figure 10c). The discordant analyses are distributed along the corresponding Stacey-Kramers common lead trend and their intercept age overlaps with the age of concordant spots.

7. $^{40}\text{Ar}/^{39}\text{Ar}$ Dating of Amphibole and Biotite

7.1. $^{40}\text{Ar}/^{39}\text{Ar}$ Methodology

The samples chosen for $^{40}\text{Ar}/^{39}\text{Ar}$ dating were collected in the Khavchig and Zalaa Uul complexes. The basic description and mineral assemblages are provided in Table 1. Detailed methodology is provided in Supporting Information S1 and analytical data in Table S3.

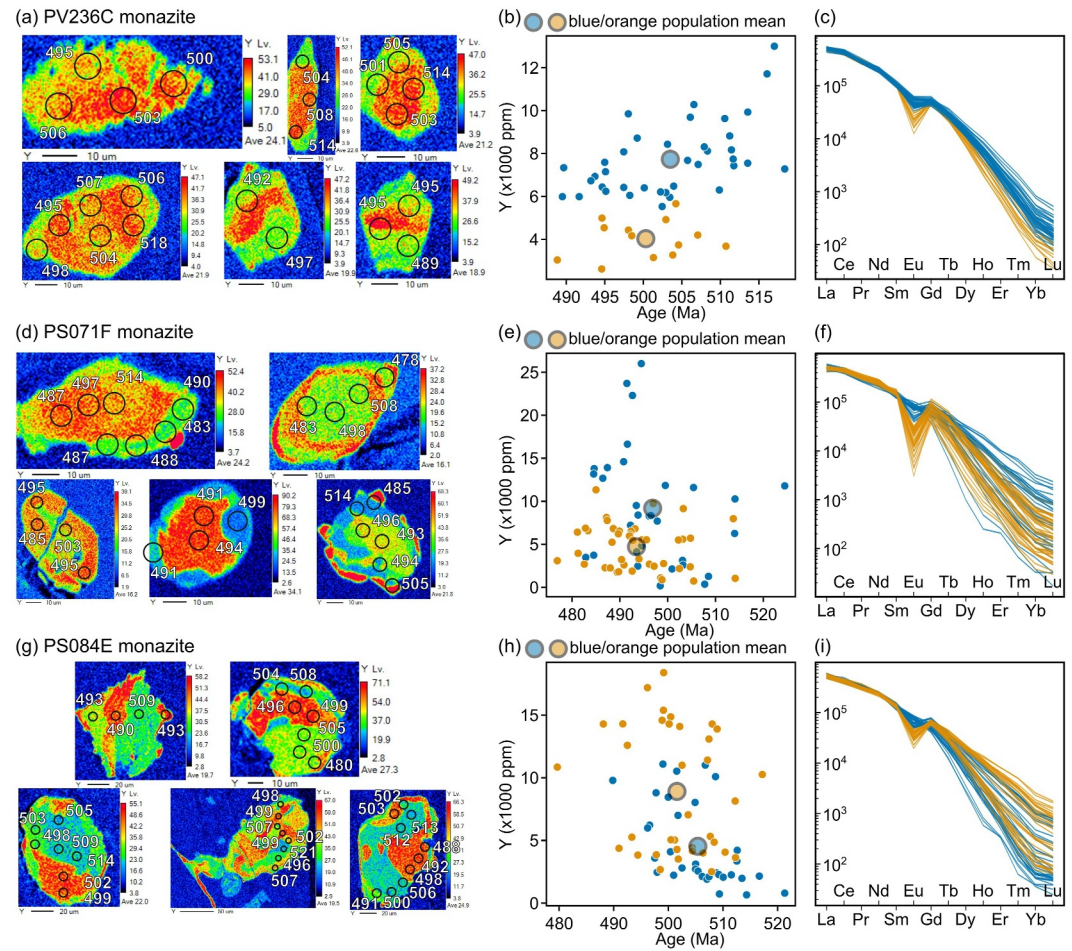


Figure 9. Monazites textures, age versus Y plots and chondrite normalized REE patterns of samples PV236C (a)–(c), PS071F (d)–(f), and PS084E (g)–(i). Orange and blue groups were classified based on Eu using cluster analysis, the color coding is identical for (b, e, h) and (c, f, i).

7.2. Results

Coarse-grained undeformed metagabbro PV210 (Zalaa Uul Complex, Figure 11a) provides saddle-shaped age spectra of amphibole grains whose pseudo-plateau ages calculated from their bases are strongly discordant, at 605.5 ± 4.5 Ma and 539.3 ± 3.5 Ma. The apparent ages of their fusion steps are also discordant and correlatively higher, at c. 638.6 Ma and c. 611.3 Ma, respectively. The $^{37}\text{Ar}_{\text{Ca}}/^{39}\text{Ar}_{\text{K}}$ spectra ($^{37}\text{Ar}_{\text{Ca}}/^{39}\text{Ar}_{\text{K}} = (\text{CaO}/\text{K}_2\text{O})/2.179$ according to Deckart et al., 1997) also have saddle shapes that roughly mimic those of the age spectra. The amplitude of these saddles is broadly correlated with that of the age spectra. The $^{37}\text{Ar}_{\text{Ca}}/^{39}\text{Ar}_{\text{K}}$ ratios of their saddle bottoms are c. 42–48 versus c. 31–35, respectively, while the ratios of the high temperature steps are broadly consistent at c. 125–130. These $^{40}\text{Ar}/^{39}\text{Ar}$ data reflect the partial recrystallization of a calcic amphibole ($^{37}\text{Ar}_{\text{Ca}}/^{39}\text{Ar}_{\text{K}} \geq 130$) older than c. 640 Ma into a more potassic amphibole ($^{37}\text{Ar}_{\text{Ca}}/^{39}\text{Ar}_{\text{K}} \leq 30$) younger than c. 540 Ma (see Supporting Information S1). The overlap of their degassing domains does not allow further clarification of their respective ages.

Amphibolite PV205 (Zalaa Uul Complex, Figure 11b) is strongly deformed and retrogressed by chlorite (Table 1). The two amphibole age spectra are highly disturbed, but have rather flat $^{37}\text{Ar}_{\text{Ca}}/^{39}\text{Ar}_{\text{K}}$ spectra (c. 8–10). There is therefore a partial decoupling between the behavior of the radiogenic system (K/Ar) and the crystalline (Ca/K) system. The only information that seems reasonable is that provided by the high temperature steps which suggest that the above-mentioned retrogression affects material at least as old as c. 712 Ma (see Supporting Information S1).

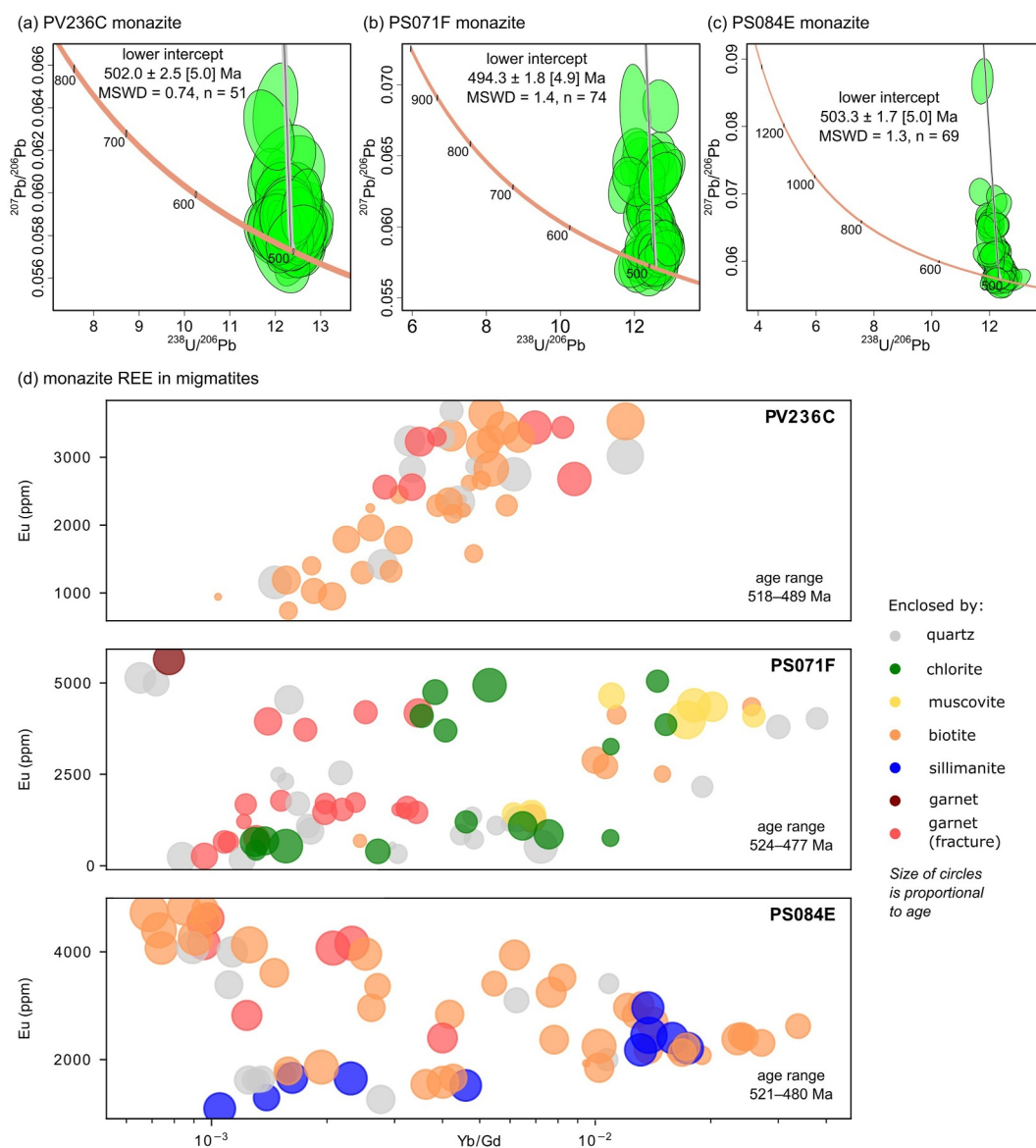


Figure 10. Terra-Wasserburg concordia plots of monazites for samples (a) PV236C, (b) PS071F, (c) PS084E. (d) REE characteristics of analysed spots. Color-coding in the Eu versus Yb/Gd plots corresponds to the enclosing mineral and size corresponds to the age.

The amphibole from amphibolite PV219 (Zalaa Uul Complex, Figure 11c) allows the calculation of a pseudo-plateau age at 470.0 ± 2.1 Ma in the high temperature steps, although it is strongly affected in the low temperature steps by degassing of younger crystalline phases characterized by lower Ca/K ratios, possibly related to alteration. The high temperature segment is representative of amphibole degassing, as suggested by the corresponding segment in the $^{37}\text{Ar}_{\text{Ca}}/^{39}\text{Ar}_{\text{K}}$ spectrum, whose ratio increases steadily from c. 7.5 to c. 10.

The amphibole from the PV226 migmatitic paragneiss (Khavchig Complex, Figure 11d) yields a plateau age of 487.0 ± 2.0 Ma. The $^{37}\text{Ar}_{\text{Ca}}/^{39}\text{Ar}_{\text{K}}$ spectrum is globally flat with ratios increasing slightly from six to eight during degassing of the amphibole. In contrast, the biotite spectrum has a staircase shape with apparent ages increasing during the degassing of the mineral, from c. 480.5 Ma in the low temperature domain to a high-temperature apparent age of 499.7 ± 2.6 Ma. The low temperature steps at c. 480 Ma are associated with a degassing peak superimposed on the main biotite degassing peak (Supporting Information S1).

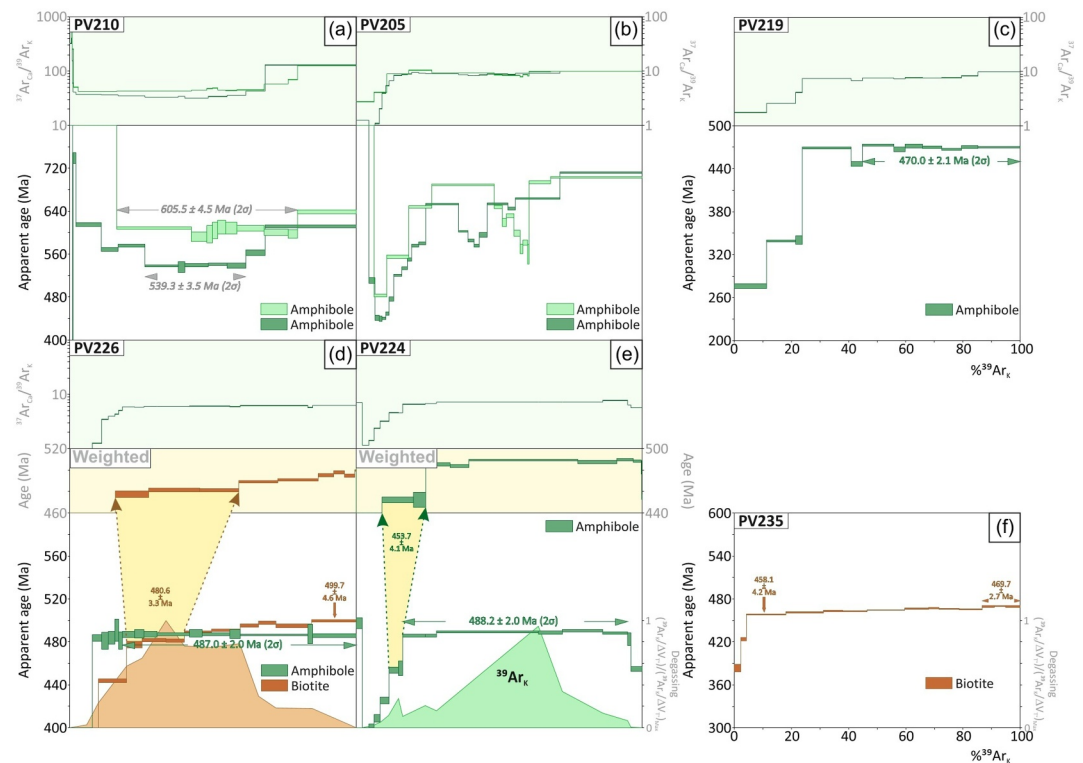


Figure 11. $^{40}\text{Ar}/^{39}\text{Ar}$ geochronology. (a) Metagabbro PV210. (b) Amphibolite PV205. (c) Amphibolite PV219. (d) Biotite-amphibole gneiss PV226. (e) Amphibolite PV224. Gneiss PV235.

The age spectrum of amphibole from amphibolite PV224 (Khavchig Complex, Figure 11e) allows the calculation of a plateau age at 488.2 ± 2.0 Ma. The corresponding flat segment in the $^{37}\text{Ar}_{\text{Ca}}/^{39}\text{Ar}_{\text{K}}$ spectrum shows slightly increasing ratios from six to eight, confirming that the calculated age is related to amphibole degassing. The hump shape of the age spectrum suggests an interaction between two radiogenic components of different ages as described in Supporting Information S1.

The biotite age spectrum of the PV235 paragneiss from the Khavchig Complex (Figure 11f) is staircase-shaped, with apparent ages increasing steadily from 458.1 ± 4.2 Ma to 469.7 ± 2.7 Ma during the degassing of the mineral. It suggests the coexistence of two distinct radiogenic components (see Supporting Information S1).

8. Discussion

8.1. Interpretation of U–Pb Dating and Relationship to the Main Migmatitic Event D_2 – M_2

Detailed investigation of the studied area revealed that the rocks record one dominant deformation and metamorphic event D_2 – M_2 , which is documented well in the structural, metamorphic and phosphate geochronological data. Despite the area preserves also relics of older evolution, they are nearly completely obscured by the dominant event D_2 – M_2 . Younger deformation events weakly modified the fold pattern and caused insignificant and static mineral growth, therefore we will focus mainly on the main event D_2 – M_2 .

Typical mineral assemblage defining the pervasive migmatitic fabric S_2 representative for metapelites of the Khavchig Complex is biotite–garnet (Mg-rich, Ca-poor)–plagioclase–quartz–ilmenite \pm K-feldspar \pm sillimanite. P–T modeling of related M_2 metamorphism revealed that S_2 formed at high temperature in the range of 760–800°C, thus far beyond the solidus of many rock types. Such peak temperature is accompanied with enhanced diffusion processes and together with deformation are capable of recrystallization of pre-peak mineral assemblages, modification of chemistry of minerals and may even open geochronological isotopic systems. On a prograde path, the first garnet starts to grow with significantly different composition than it has at partial melting

conditions (e.g., Štípská et al., 2020). Therefore the chemically homogeneous and smaller garnets of the samples PV236C and PS071F (<2 mm) can be interpreted as a product of peak temperature overprint of the original prograde zoning (i.e., still preserved in the >5 mm large garnet in the sample PS084E).

The U–Pb dating of phosphates yields homogeneous single-peak Cambrian ages. Because the protoliths of the migmatites are Neoproterozoic (Bold et al., 2016; Soejono et al., 2025), the monazite ages are interpreted in terms of the metamorphic evolution of the area. U–Pb dating of monazite in three paragneiss samples gives uniform ages. Two samples in the west give overlapping ages in the range of c. 505–500 Ma, while the eastern sample gives a slightly younger age around c. 494 Ma. There is no significant difference between the age of the monazite enclosed in garnet and sillimanite porphyroblasts or in the matrix, nor in relation to their relatively variable REE pattern. Additionally the grains have complex textures (visible in Y maps in Figure 9) pointing to the complex recrystallization processes of the grains, but all spots yield overlapping ages within error (single spot has an error of >10 Ma, see Supporting Information S1). Same age for grains which are inclusions in porphyroblasts as well as for grains in the matrix also suggests that there was no significant low-grade overprint nor preserved prograde stage (both leading to matrix younger than inclusions). The homogeneity of the U–Pb ages is in agreement with the high-temperature environment which may lead to opening of the U–Pb isotopic system, but keeping the chemical record of multistage growth and recrystallization. Decoupling of the age systematics from the chemical record of the grains is common in monazites and has been described in many situations (e.g., Grand'Homme et al., 2016; Jouvent et al., 2023). Such observations underline the interpretation that the late Cambrian age reflects the timing of the major anatectic event D_2 – M_2 . Whether the different textural domains formed during the relatively short-lived single process (corresponding to the D_2 – M_2 event) or whether some of the zoning represents older grains whose age was reset during the D_2 – M_2 , can not be resolved.

The only exception is sample PV236C, where HREE correlates with Eu anomaly (Figures 9a–9c and 10d). The Yb/Gd ratio in monazite is usually linked to the garnet, which strongly partitions HREE. Simultaneous garnet and monazite growth yields low HREE, while garnet breakdown produces high HREE ratio in monazite (e.g., Rubatto et al., 2013). Analogously, the Eu content in monazite is dependent on the relationship to feldspar, which partitions Eu. When monazite grows after or together with feldspar, monazite is depleted in Eu, when feldspar breaks down or is absent in the assemblage, the Eu anomaly in monazite is missing (e.g., Wang et al., 2015). In the case of sample PV236C, the occurrence of K-feldspar at the expense of muscovite is probably the key reaction affecting the Eu systematics. Therefore the low Eu associated with low HREE can be interpreted as a high-temperature monazite growth (HREE partitioned to garnet, K-feldspar produced at the expense of muscovite). Higher Eu and higher HREE content can be interpreted either as an older or prograde stage (lower garnet mode, absence of K-feldspar in the assemblage), or post-peak growth due to decreasing garnet mode and decreasing mode of K-feldspar. However pre- or post-peak timing of the lower Eu and lower HREE monazite growth can not be assessed because it is within the error of the U–Pb dating method.

Another perspective comes from the key outcrop PV229 showing variable relationships of leucogranite dikes to the S_1 and S_2 fabrics. Some of them are parallel to S_1 , others occur as folded leucogranite dikes with axial planes parallel to S_2 and some dikes are subparallel to S_2 and commonly boudinaged. Such structural relationships are typical examples of pre- to syn- D_2 emplacement of melts that can be therefore considered as partial melts of the high-grade M_2 – D_2 event. The dated boudinaged dike of the leucogranite from this outcrop contains oscillatory-zoned monazite and xenotime, typical for magmatic origin (e.g., Broussolle et al., 2015; Rubatto et al., 2013; Schulz, 2021; Townsend et al., 2001). In places, the oscillatory-zoned monazite and xenotime cores are surrounded or embayed by BSE-structureless rim (Figure 8a), indicative of dissolution-precipitation process (e.g., Kelly et al., 2012 and references therein). However, both texturally different domains in these monazite and xenotime grains give within the error indistinguishable ages (ranging c. 510–495 Ma for xenotime and c. 500–495 Ma for monazite), suggesting a (re)crystallization of grains in the dike within the resolution of the U–Pb dating method. Similarly, the chemically distinct monazite cores, embayments and rims in gneiss samples provide within the error comparable ages (Figures 9 and 10). Therefore we conclude that crystallization of monazite/xenotime from melt, and/or metamorphic crystallization and their subsequent metamorphic modification occurred in a short time interval and indicates semi-contemporaneous magmatic and metamorphic processes during the peak of M_2 – D_2 .

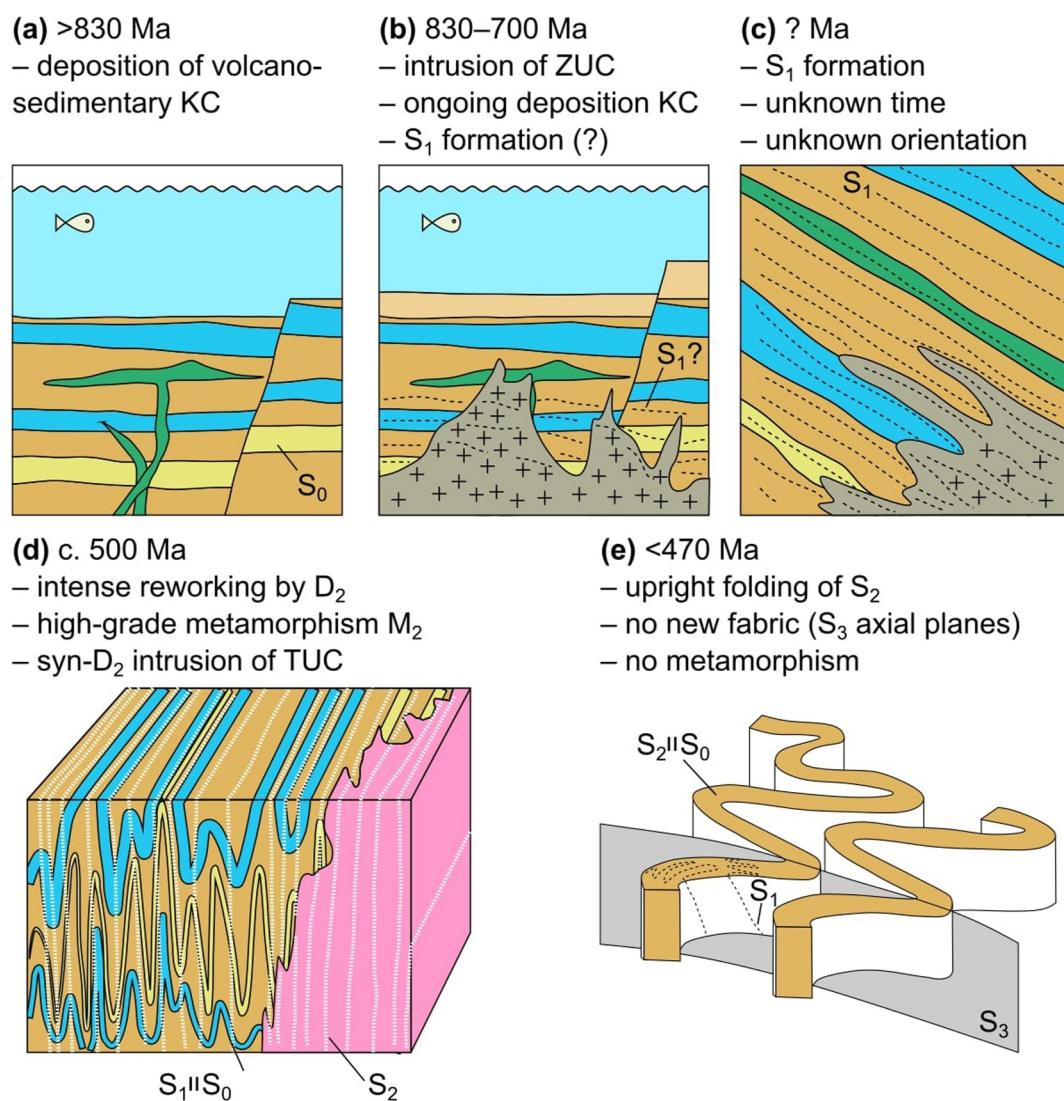


Figure 12. Schematic sequence of main events in the studied area. (a) Passive margin sedimentation (extension). (b) Intrusion of Zala Uul Complex into the passive margin sequence. (c) Formation of S_1 fabric with unknown orientation at unknown time between Tonian intrusion of Zala Uul Complex and Cambrian deformation. (d) Main deformation and metamorphic event M_2 – D_2 . (e) Post-metamorphic folding of the whole sequence. Color coding as in Figure 1c.

8.2. Tectonic Evolution of the Altai Area

The tectonic evolution of the studied rocks can be divided into several stages that can be partially linked with the identified deformation events D_1 – D_4 . They are recorded in the rocks at various intensities and the sequence of major events is illustrated in Figure 12.

The evolution of the area started with the deposition of the oldest members of the volcano-sedimentary Khavchig Complex, prior to the intrusion of the Zala Uul Complex (c. 830–700 Ma), and with sedimentation continuing later on (Figures 12a and 12b). The first metamorphic fabric S_1 occurs both in the Zala Uul Complex and Khavchig Complex and marks the existence of an early D_1 event (Figure 12c). However, the U–Pb ages presented in this work do not contain any age group older than M_2 – D_2 . This may result from complete recrystallization of any potential M_1 monazite under high temperature during M_2 event ($>750^\circ\text{C}$). Alternatively, it can also reflect the low-temperature conditions of M_1 , insufficient to form monazite. The S_1 fabric had to be formed sometime before the late Cambrian because the S_1 fabric is present in the late Cambrian Zala Uul Complex but is missing in the

Tonian Teeg Uul Complex. However, no specific constraints on the earliest deformation stage can be obtained from this study.

Fold axes L_2 show variable orientations in the stereonet (Figure 3) with a subvertical NNE plunging maximum, suggesting possibly steep orientation of S_1 prior to the D_2 event. However, the reconstruction of the original orientation of fabric before the superposed event is problematic when the younger fabric records a high strain. It has been shown that fold axes are prone to rotation into the stretching direction of the younger event (e.g., Alsop et al., 2010; Carreras, 2001; Peřestý et al., 2020). This would imply that in our case it was rather the D_2 stretch that was subvertical. Orientation of S_1 fabric in Figure 12c is therefore only schematic.

The M_2 event also led to a near-complete recrystallization of M_1 mineral assemblages. The exception is the sample PS084E, which preserves a relic metamorphic stage represented by Ca-rich cores of large garnet porphyroblasts enclosing rutile, muscovite and chlorite. As argued in the P–T modeling section, quantitative estimates of P–T conditions are not reasonable. However, qualitative behavior of metapelitic systems indicate that relics of prograde stage are typical for subsolidus conditions and rather LT–HP metamorphic environments. It should be emphasized, that any direct link of these assemblages to the S_1 fabric is uncertain, and they can similarly represent only a prograde stage of the M_2 metamorphism.

On the other hand, the late Cambrian pervasive migmatization M_2 – D_2 is well constrained (Figure 12d). The melting was clearly syn-kinematic with the S_2 fabric and the range of monazite and xenotime ages may be interpreted as the time span of the high-temperature conditions (c. 510–495 Ma). The Teeg Uul orthogneiss, which intruded at c. 503 Ma into the partially molten environment, is also penetratively reworked by D_2 deformation, indicating that large magmatic portions have been emplaced during the course of D_2 – M_2 . The pressure estimates around 0.55–0.80 GPa place the M_2 – D_2 to a depth level of c. 20–30 km, into the middle crust with elevated metamorphic gradient in the range of 25–40°C/km. The S_2 fabric was folded at the km-scale by F_3 folds (Figure 3), but the S_2 limbs remained uniformly subvertical suggesting that the pre- D_3 orientation of the S_2 fabric was also subvertical as shown in Figure 12d.

Since the main syn-intrusive migmatitic fabric is subvertical, an extensional regime that can cause the necessary heating of the middle crust is rather unlikely and an external heat source is required. The best possible source of heat is the advection from the voluminous late Cambrian magmatism, which was attributed by Soejono et al. (2023) to the protracted activity of the vast Ikh Mongol Arc system from c. 525 to 480 Ma (Janoušek et al., 2018). The absence of any deformation fabric associated with overprinting mineral assemblages suggests that the cooling of the massif occurred probably in a static environment. On the other hand, the heterogeneously developed static retrogression characterized by a replacement of sillimanite and K-feldspar by fine-grained muscovite aggregates, replacement of biotite by chlorite + ilmenite/rutile \pm muscovite and secondary chloritization of garnet along cracks can be correlated with some of the later stages of the post- M_2 – D_2 cooling.

The last deformation increments are associated with D_3 and D_4 folding (Figure 12e), which seem to take place at (sub)greenschist-facies conditions, and without any clear mineral growth that would form a new mechanical anisotropy in the rocks. The age of these two events is unknown, but they may be responsible for the final thickening of the crust, causing erosion of the hanging wall of the mid-crustal migmatites. Events D_3 and D_4 may also cause the relatively widespread retrogression of mineral assemblages to the southwest toward the contact with the Lake Zone and along the northern boundary fault as shown in Figure 1c.

8.3. Interpretation of Ar–Ar Data

The data set produced by the $^{40}\text{Ar}/^{39}\text{Ar}$ experiments is highly heterogeneous. For interpretation we use only the plateau ages of amphiboles from samples PV219, PV226, and PV224 and the high temperature pseudo-plateau age of the staircase age spectrum of biotite from sample PV235. Discussion and possible interpretation of secondary disturbances of all the samples is provided in Supporting Information S1.

The amphiboles yielding plateau ages are located in the central (PV226, PV235) and eastern (PV219 and PV224) parts of the study area. Their isotopic closure ages of c. 490–485 Ma (but down to c. 470 Ma in the far east) are 15–20 Myr younger than the nearby monazite ages. They are therefore best interpreted as cooling ages of the rocks, reflecting the effective closure of the amphibole crystal lattice to $^{40}\text{Ar}^*$ diffusion (to c. 550–650°C, see discussion in Tremblay et al., 2020) from the peak temperature conditions of M_2 (>750°C). The high temperature pseudo-plateau age of c. 470 Ma provided by biotite from sample PV235, with an isotopic closure temperature usually

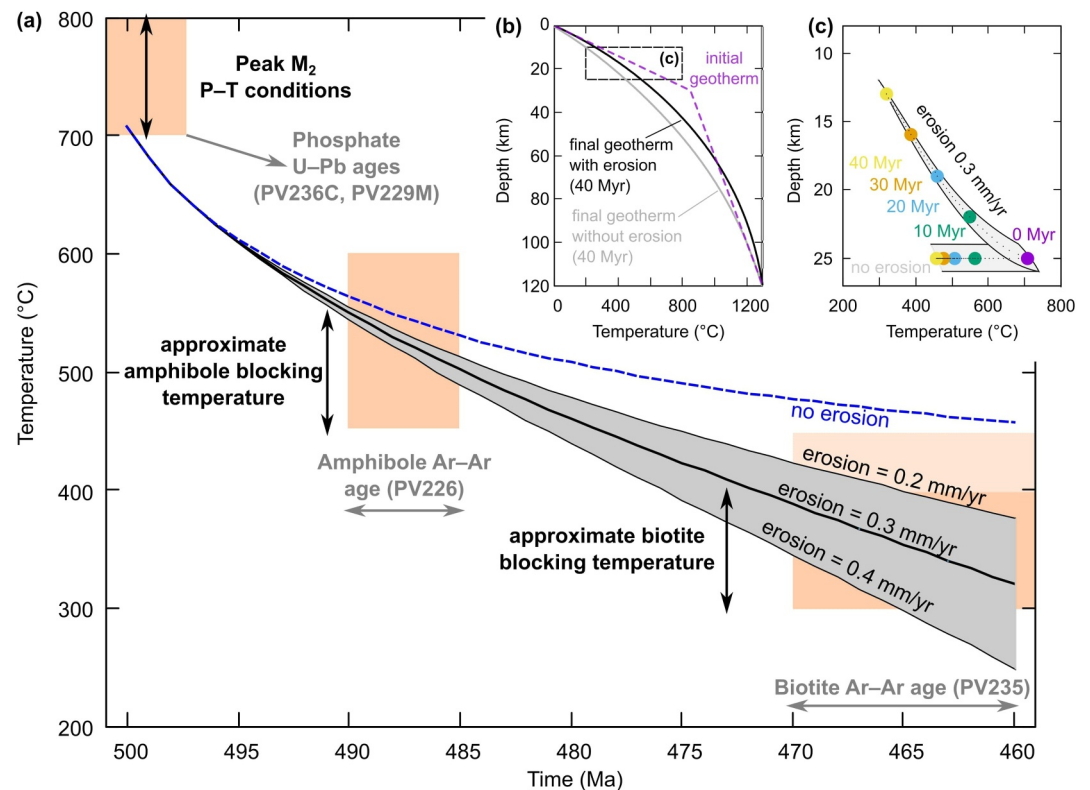


Figure 13. Cooling history of the area. (a) Modeled cooling history with starting depth 25 km and variable erosion rates. (b) Initial geotherm (dashed violet) and its relaxation after 40 Myr with erosion (black) and without erosion (gray). (c) Temperature-depth for erosion rate 0.3 mm yr⁻¹ and without erosion. Gray regions show variations for samples with initial depth of 24–26 km.

accepted in the range of 350–450°C (see discussion in Tremblay et al., 2020), can also be interpreted as a cooling age. It should be noted that the concept of isotopic closure temperature should be treated with caution (see comment in Supporting Information S1).

8.4. Cooling History Tested Against Thermal Model

In the study area, the cooling of the high-grade complex is constrained by U–Pb monazite and ⁴⁰Ar/³⁹Ar dating of minerals with contrasting blocking temperatures (Figure 13). The observed cooling history is tested against a one-dimensional thermal numerical model using the ASPECT code (Bangerth et al., 2022; Heister et al., 2017; Kronbichler et al., 2012). The model is described in more detail in Supporting Information S1, where several cooling regimes were tested (different initial geotherms together with different erosion rates under shortening, under extension, and without deformation).

In the calculations, we consider the data from the most-explored central part of the Khavchig Complex. The U–Pb ages of phosphates around c. 500 Ma (PV236C, PV229M, Figure 13a) reflect the thermal peak above 700°C, followed by amphibole ⁴⁰Ar/³⁹Ar age of c. 490–485 Ma (PV226, Figure 13a) using blocking temperatures c. 450–600°C and biotite age of c. 470–460 Ma (PV235, Figure 13a) using blocking temperature c. 300–450°C. We intentionally consider wide ranges of blocking temperatures as they are dependent on various (and generally unknown) parameters, as described in Supporting Information S1. The aim is not to find a precise cooling history as possible, but to identify feasible first-order cooling scenarios.

The results show that if we assume thermal relaxation of an elevated arc-like geotherm without deformation and without erosion from the depth of c. 25 km inferred from peak pressure conditions (Figures 13b and 13c), the cooling in later stages is too slow compared to the data (Figure 13a, blue dashed line). On the other hand, taking into account relatively conservative erosion rates around c. 0.3 mm yr⁻¹ the model reproduces the observed data

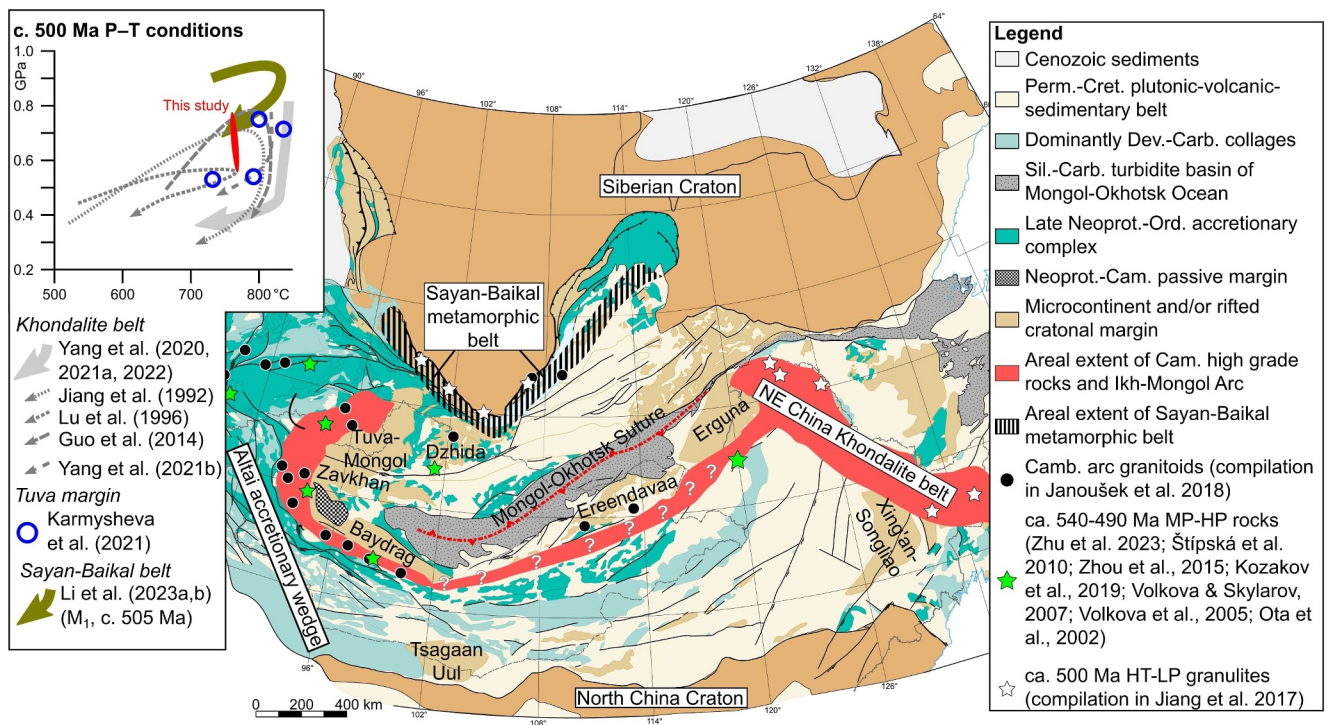


Figure 14. Geological map showing the proposed of Cambrian–Ordovician magmatic and metamorphic rocks (red). The continuation of the belt along Ereendavaa block is speculative due to the lack of data. Modified after Li et al. (2023a, 2023b). Top left inset is a compilation of available P–T estimates for c. 500 Ma high-grade metamorphism in Khondalite belt, Tuva margin and Sayan-Baikal belt (Guo et al., 2014; Lu et al., 1996; Ota et al., 2002; Volkova & Sklyarov, 2007; Volkova et al., 2005; Yang et al., 2020; Yang, Yang, et al., 2021; Yang, Zheng, et al., 2021).

well. If the lateral shortening, corresponding to D₂ phase, is taken into account, the cooling rate decreases (Supporting Information S1). Such a situation corresponds well to the early stages of thermal evolution but is incompatible with the late stages. In contrast, if an extensional regime is considered, the cooling is faster (Supporting Information S1), which could theoretically explain the data for the late stages. However, extension is not supported by the geological observations presented in this paper. To sum up, the observed temperature-time data are compatible with the cooling of an arc undergoing shortening in the early stage and moderate erosion in the late stage.

8.5. Regional Correlations With Late Cambrian Orogens in CAO

This work describes the contractional MP–HT event associated with the intrusion of Ikh Mongol Arc granitoids along the southern margin of the Zavkhan Block. However, it is important to note that the intrusion of these granitoids was preceded by the HP–LT event in the nearby Urgamal region at the western margin of the Zavkhan Block. There, c. 520 Ma eclogites with estimated P–T conditions of ~2.2 GPa and 560°C were interpreted as a part of a large subduction wedge (Zhu et al., 2023). Similar P–T conditions of ~2.0–2.2 GPa and 590–610°C for Zamtyu Nuruu eclogites dated to c. 535 Ma, spatially related to Ikh Mongol Arc granitoids, were reported from the southern border of the Baidrag Block (Buriánek et al., 2017; Skuzovatov, 2021; Štípská et al., 2010). Altogether, the occurrences of HP rocks along the external margins of the Zavkhan and Baidrag blocks point to the existence of c. 535–520 Ma oceanic suture, discontinuously intruded by the Ikh Mongol Arc granitoids associated with granulite to amphibolite-facies metamorphism at around 510–470 Ma.

The tectonometamorphic evolution of the southern margin of the Zavkhan Block can be correlated with tectono-metamorphic records in other parts of the Mongolian Collage (Figure 14). The existence of c. 530 Ma MP/HP metamorphism preceding the HT–LP metamorphism was reported for the Moren Complex of the Tuva-Mongolia Block by Kozakov et al. (2019). Subsequent HT–LP granulite-facies metamorphism, widespread migmatization and granitic magmatism have been identified in the Erzin Zone at the western margin of the Tuva-Mongolia

Block. There, the age of the thermal peak has been determined by U–Pb zircon dating of syn-tectonic granitoids to c. 510–490 Ma (Karmysheva et al., 2017, 2021; Kozakov et al., 1999) and 490 ± 2 and by 477 ± 6 Ma U–Pb zircon ages of syn-collisional granites from the Dzhida Zone (Gordienko et al., 2012). This event was interpreted to result from the collision with the Tannuola-Khamsara island-arc system (Karmysheva et al., 2021; Kozakov et al., 2001).

The comparable late Cambrian–early Ordovician event is well documented in the Sayan–Baikal Belt flanking the southern margin of the Siberian Craton (Donskaya et al., 2000). The emblematic example, the Olkhon Terrane, shows peak pressure conditions of 0.7–1.1 GPa at 770–877°C for the granulite-facies metamorphism of the Chernorud Zone and ~ 0.6 –0.8 GPa at 630–710°C for the amphibolite-facies Anga-Sakhurta Zone dated at c. 507–470 Ma (Donskaya et al., 2017; Gladkochub et al., 2008; Li et al., 2009; Sklyarov et al., 2020).

However, Li et al. (2023a) proposed that the prograde metamorphism of the granulite-facies rocks of the Olkhon Terrane started already at c. 535 Ma as also indicated by c. 530 Ma age of adjacent migmatites (Vladimirov et al., 2011). This metamorphic event can be correlated to deposition of youngest c. 530 Ma detrital zircons of the Anga-Sakhurta Zone (Donskaya et al., 2017, 2022) together with deposition of c. 540–530 Ma detritus in the foreland basin of the Siberian platform (Motova et al., 2024). Temporal coincidence between the sedimentation and metamorphic processes corresponds well to models of erosion of extruded orogenic cores both at the pro- and retro-side of orogenic wedges (Malavieille, 2010; Willett, 1999). Li et al. (2023a) further reported that the granulites and migmatites of the Olkhon Terrane reached peak pressure conditions of 0.8–0.9 GPa at c. 500 Ma. This finding corroborates with c. 500 Ma age for syn-tectonic granite from the Derba Zone (Nozhkin et al., 2005) and c. 495 Ma syn-tectonic granite from the Khamar Daban Complex of the Sludyanka Zone (Barash et al., 2006). Finally the granulites and migmatites of the Olkhon Terrane were affected by a second phase of HT–LP metamorphism at ~ 0.5 GPa at around 470–440 Ma associated with regional syn-extensional mafic and granitic magmatism dated by zircon and monazite at c. 475–445 Ma (Fedorovsky et al., 2010; Makrygina et al., 2014; Mikheev et al., 2017). The tectonic evolution of the Olkhon terrane was terminated by c. 430–400 Ma sinistral shearing at greenschist-facies as indicated by numerous Ar–Ar cooling ages (Fedorovsky et al., 2020; Li et al., 2023a; Travin et al., 2009; Vladimirov et al., 2011).

The late Cambrian granulite-facies metamorphism has been documented in high-grade gneisses outcropping in the Erguna, Songliao, Xing'an, Jiamusi and Khanka microcontinental blocks of the eastern CAOB (e.g., Wilde et al., 2000; Zhou & Wilde, 2013; Zhou, Wilde, Zhang, Ren, & Zheng, 2011; Figure 14). These occurrences were collectively assigned to the “NE China Khondalite Belt” and interpreted as an eastern continuation of the Sayan–Baikal metamorphic belt (Wilde, 2015; Zhou, Wilde, Zhang, Zhao, et al., 2011). There, the granulites of the Mashan Complex of the Jiamusi Massif show a clockwise P–T path with peak pressure ~ 0.74 GPa at 800–850°C and retrograde conditions at the stability field of cordierite at 0.45–0.55 GPa (Jiang, 1992; Yang et al., 2022, 2023). Amphibolite-facies conditions of 550–650°C and 0.6–0.7 GPa dominated less metamorphosed parts of the massif. Very important was the discovery of blueschists (0.9–1.1 GPa at 320–450°C) cross-cut by a granite dikes dated at c. 490 Ma, and cropping out on the southern margin of the Erguna Block (Zhou et al., 2015). The age of blueschist facies metamorphism was indirectly constrained at c. 510–490 Ma, and indicates a HP event preceding the metamorphic reequilibration associated to early Ordovician magmatism. In summary, the geochronological data of granulites and granitoids of the 1,300 km long Khondalite Belt shows a relatively short interval of metamorphic and magmatic activity ranging from c. 500 to 480 Ma (Zhou, Wilde, Zhang, Ren, & Zheng, 2011; Zhou, Wilde, Zhang, Zhao, et al., 2011; Zhou et al., 2010; Yang et al., 2022), with an age peak at c. 495 Ma in the Xing'an, Erguna and Jiamusi blocks, and c. 520–480 Ma interval for the southernmost Khanka Block.

This data is compatible with the Zavkhan margin, which shows c. 500 Ma age of the thermal peak and short c. 520–480 Ma orogenic and cooling history. In addition, the continental blocks forming the southern part of the Mongolian Collage (Tuva-Mongolia, Zavkhan, Baidrag) show remarkable similarity in the age of the late Tonian and Cambrian–Ordovician magmatic complexes with the continental blocks of the NE China (Erguna, Xing'an, Songliao, Jiamusi-Khanka), indicating the same Rodinian break-up and peri-Siberia active margin events (Soejono et al., 2023). These blocks also show large similarity in presence of Mesoproterozoic and Neoproterozoic zircon peaks (Zhou et al., 2018).

Altogether, the short-lived two-stage c. 530–480 Ma metamorphic and magmatic evolutions of the Zavkhan, Baydrag and Tuva-Mongolia are not compatible with long-lived and multi-stage 530–400 Ma Sayan-Baikal orogen. On the other hand, the studied Khavchig Complex shows great similarity with the metamorphic

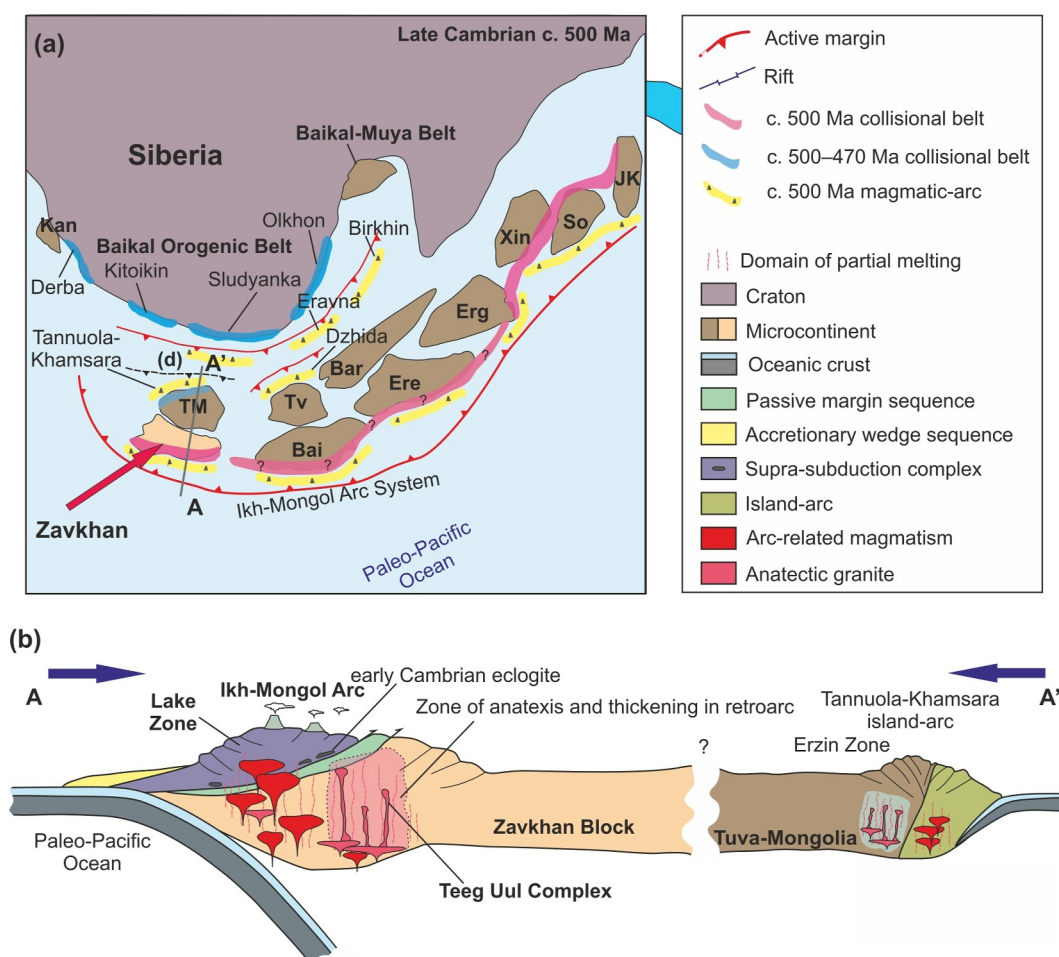


Figure 15. Paleogeography and tectonic model of the Zavkhan margin in frame of CAOB. (a) Late Cambrian peri-Siberian position of Mongolian microcontinents. (b) Interpreted late Cambrian cross section through B–B' in (a).

conditions and timing of metamorphism in the NE China Khondalite Belt (Figure 14) and the Tuva-Mongolia Block further north. The existence of an early Cambrian eclogite wedge followed by short-lived Cambrian–Ordovician HT metamorphism and Japan-type arc magmatism may indicate the existence of a single orogenic belt extending from NE China through SW Mongolia toward Russia. This suggestion is not compatible with the commonly proposed connection of the NE China Khondalite Belt with the granulite belt of the Sayan Baikal Orogen (e.g., Wilde, 2015; Zhou et al., 2018). In contrast, our favored scenario corroborates an unconventional model of contiguous S-shaped string of Precambrian terranes forming the so-called “Hingan” orocline in NE China and Mongolian Orocline in west Mongolia (Yakubchuk, 2017). Similarly, Liu et al. (2023) proposed a continuity of an early Paleozoic arc shaping the so-called NE China Orocline (the Hingan orocline of Yakubchuk) with the curved Ikh Mongol Arc in the west Mongolia.

8.6. Geodynamic Model of the Mongolian Collage Formation

The above-discussed kinematics, P–T and geochronological constraints from the southern Zavkhan margin and comparisons with other areas in the CAOB provide new insights into the geodynamic evolution of the Mongolian Collage. Thus the proposed tectono-thermal sequence is discussed here in a broader geodynamic context. The original orientation, grade and age of the first metamorphic fabric S_1 , preserved in the rocks of the Khavchig Complex and Zalaa Uul Complex, are unfortunately unknown due to later pervasive syn- D_2 reworking and pervasive M_2 metamorphism. We can only speculate whether the first and relictual metamorphic fabric may have

formed during the Tonian to Cryogenian extensional event, documented by sedimentary and magmatic records throughout the southwestern margin of the Zavkhan Block (Bold et al., 2016; Kovach et al., 2021; Levashova et al., 2010; Soejono et al., 2023).

As described above, the overall supra-subduction regime started at latest in the early Cambrian, as well-documented by occurrences of c. 530 Ma HP rocks along the outer border of the Mongolian Collage. Formation of the giant Paleo-Pacific subduction system (Figures 15a and 15b) and associated contraction of the whole Mongolian Collage led to a closure of oceanic basins located between the Siberia and SE Asia-type archipelago (e.g., Gordienko et al., 2007, 2010; Sukhbaatar et al., 2024; Štípská et al., 2024).

Subsequent continuation of the convergent regime is deduced here from sub-vertical geometry of the high-grade S_2 fabric around c. 505–495 Ma. The peak P–T conditions of associated M_2 clearly indicate that crustal thickening (D_2) operated at an elevated thermal regime. The late Cambrian age for M_2 – D_2 syn-tectonic anatexis is effectively identical to the peak of magmatic activity in the Khantaishir Magmatic Complex in the direct vicinity of the study area (Janoušek et al., 2018), as well as the age of the entire Ikh-Mongol Arc System reported from several microcontinents of the Mongolian Collage (for review see Soejono et al., 2023; Figures 14 and 15). It has been shown that the D_2 deformation was accompanied by massive crustal melting and intrusions of syn-kinematic granites in the study area at c. 500 Ma (Soejono et al., 2023). The temporal and spatial coincidence of horizontal shortening and arc magmatism in the Zavkhan margin suggest a genetic link between these two events and, as discussed above, it can explain the high geothermal gradient in the compressional tectonic regime. Analogous hinterland arc-parallel zones, facilitating significant horizontal shortening, have been documented for example, in the Southern Apennines (Hippolyte et al., 1995), Sierran continental margin in California (Ducea, 2001; Dunne & Walker, 2004) and modern Andes (DeCelles et al., 2009). Like the southern margin of the Zavkhan Block, these examples of contractional deformation were contemporaneous with an increased magmatic arc activity (DeCelles et al., 2009; Ducea et al., 2015). Massive crustal anatexis of the host rocks of the magmatic arc may cause thermal softening and a decrease in the strength of the crust. These conditions facilitate the formation of hot and weak crustal zones that are prone to strain localization and can be easily shortened and thickened.

Possible early Paleozoic orogenic belt illustrated in Figures 14 and 15 most likely formed as a result of c. 30 Myr advancing mode of the Paleo-Pacific Ocean and defines the terminal stage of the Ediacaran–Cambrian amalgamation of the entire Mongolian Collage. This belt is represented by high-grade c. 500 Ma metamorphic complexes related to the formation of the Ikh Mongol Arc as presented in this work. Commonly, these high-grade complexes are discontinuously accompanied by c. 530 Ma HP metamorphic remnants that are later overprinted by c. 500 Ma HT metamorphism (Figures 14 and 15). This region developed at the direct contact with the exterior Paleo-Pacific (Panthalassa) Ocean subducting beneath the accreted Mongolian Collage. The above-described spatial distribution of c. 500 Ma HT metamorphism, often paired with the coeval arc magmatism, suggests a systematic repetition of such tectono-magmatic zoning across a large domain between the southern margin of the Zavkhan Block and the southern edge of Siberia (Figures 15a and 15b).

9. Conclusions

The c. 500 Ma event expresses a terminal stage of collision of the archipelago with Siberia, hallmarking the formation of the larger Siberia continent at the time (e.g., Cocks & Torsvik, 2007).

- The migmatization of the southern margin of the Zavkhan Block took place at ~760–800°C and 0.55–0.80 GPa at c. 505–495 Ma. The metamorphism was coeval with intrusion of a late Cambrian arc.
- Horizontal, syn-convergent shortening of the arc domain is documented by syn-tectonic emplacement of leucogranite sheets in the axial planar cleavage of upright folds constrained by U–Pb monazite and xenotime 505–500 Ma ages.
- The cooling of the massif recorded by Ar–Ar biotite and amphibole ages is consistent with early stage lateral shortening of hot edifice followed by moderate erosion in the late stage.
- Comparison with the other metamorphic and magmatic belts from NE China revealed remarkable similarities in age, metamorphic conditions and close spatial relationship to widespread Cambrian–Ordovician Ikh Mongol Arc magmatism overprinting slightly older high-pressure rocks. All that allows proposing an existence of a continuous orogenic belt that flanks the Precambrian microcontinents of the Central Asian Orogenic Belt.

Data Availability Statement

Heat transport computations were done using the ASPECT code version 2.4.0 (Bangerth et al., 2022; Heister et al., 2017; Kronbichler et al., 2012) and are further described in Supporting Information S1. Thermodynamic modeling was performed using MAGEMin (Riel et al., 2022). Structural data have been collected by the author team and were processed by the APSG module (<https://doi.org/10.5281/zenodo.593586>, Lexa, 2023). The representative mineral analyses are provided in Table S1., the monazite and xenotime U-Pb data were processed using the online version of IsoplotR (Vermeesch, 2018) and analytical data are provided in Table S2. Ar–Ar analytical data are provided in Table S3.

Acknowledgments

This study was funded by the Czech Science Foundation (GAČR EXPRO) project 19-27682X to K. Schulmann and by Research Project no. 329805 (Strategic Research Plan of the Czech Geological Survey—DKRVO/ČGS 2023–2027). We thank to anonymous reviewer and Tatiana Donskaya for constructive reviews which significantly helped to improve the final version of the manuscript. Finally we acknowledge Djordje Grujic for his editorial work. Open access publishing facilitated by Ceska Geologicka Sluzba, as part of the Wiley - CzechELib agreement.

References

- Aguilar, C., Štípská, P., Schulmann, K., Kylander-Clark, A. R., Lexa, O., Sukhbaatar, T., et al. (2024). Carboniferous Barrovian to Permian Buchan-type metamorphic cycles in the Mongolian Altai Zone: Implication for pressure cycles in accretionary orogens. *Journal of Metamorphic Geology*, 42(7), 979–1033. <https://doi.org/10.1111/jmg.12777>
- Alsop, G. I., Cheer, D. A., Strachan, R. A., Krabbendam, M., Kinny, P. D., Holdsworth, R. E., & Leslie, A. G. (2010). Progressive fold and fabric evolution associated with regional strain gradients: A case study from across a Scandian ductile thrust nappe, Scottish Caledonides. *Geological Society, London, Special Publications*, 335(1), 255–274. <https://doi.org/10.1144/SP335.12>
- Badarch, G., Cunningham, W. D., & Windley, B. F. (2002). A new terrane subdivision for Mongolia: Implications for the Phanerozoic crustal growth of Central Asia. *Journal of Asian Earth Sciences*, 21(1), 87–110. [https://doi.org/10.1016/S1367-9120\(02\)00017-2](https://doi.org/10.1016/S1367-9120(02)00017-2)
- Bangerth, W., Dannberg, J., Fraters, M., Gassmoeller, R., Glerum, A., Heister, T., et al. (2022). ASPECT v2.4.0 (version v2.4.0). *Zenodo*. <https://doi.org/10.5281/zenodo.6903424>
- Barash, I. G., Sal'nikova, E. B., Reznitsky, L. Z., Kotov, A. B., Kovach, V. P., Yakovleva, S. Z., & Fedoseenko, A. M. (2006). Age relations between metamorphism of the Slyudyanka granulite and the Khamar Daban zoned metamorphic complexes: Evidence from U-Pb geochronological data. *Doklady Earth Sciences*, 409(2), 905–908. <https://doi.org/10.1134/S1028334X06060158>
- Bold, U., Crowley, J. L., Smith, E. F., Sambuu, O., & Macdonald, F. A. (2016). Neoproterozoic to early Paleozoic tectonic evolution of the Zavkhan terrane of Mongolia: Implications for continental growth in the Central Asian orogenic belt. *Lithosphere*, 8(6), 729–750. <https://doi.org/10.1130/L549.1>
- Broussole, A., Štípská, P., Lehmann, J., Schulmann, K., Hacker, B. R., Holder, R., et al. (2015). *P–T–t–D* record of crustal-scale horizontal flow and magma-assisted doming in the SW Mongolian Altai. *Journal of Metamorphic Geology*, 33(4), 359–383. <https://doi.org/10.1111/jmg.12124>
- Buriánek, D., Schulmann, K., Hrdličková, K., Hanžl, P., Janoušek, V., Gerdes, A., & Lexa, O. (2017). Geochemical and geochronological constraints on distinct Early-Neoproterozoic and Cambrian accretionary events along southern margin of the Baydrag Continent in western Mongolia. *Gondwana Research*, 47, 200–227. <https://doi.org/10.1016/j.gr.2016.09.008>
- Buriánek, D., Soejono, I., Schulmann, K., Janoušek, V., Hanžl, P., Čáp, P., et al. (2022). Subduction-controlled temporal and spatial variations in early Palaeozoic sedimentary and volcanic record of the Mongol–Altai Domain. *Journal of Asian Earth Sciences*, 230, 105182. <https://doi.org/10.1016/j.jseas.2022.105182>
- Carreras, J. (2001). Zooming on Northern Cap de Creus shear zones. *Journal of Structural Geology*, 23(9), 1457–1486. [https://doi.org/10.1016/S0191-8141\(01\)00011-6](https://doi.org/10.1016/S0191-8141(01)00011-6)
- Chen, M., Sun, M., Buslov, M. M., Cai, K., Zhao, G., Zheng, J., et al. (2015). Neoproterozoic–middle Paleozoic tectono-magmatic evolution of the Gorny Altai terrane, northwest of the Central Asian Orogenic Belt: Constraints from detrital zircon U–Pb and Hf-isotope studies. *Lithos*, 233, 223–236. <https://doi.org/10.1016/j.lithos.2015.03.020>
- Cocks, L. R. M., & Torsvik, T. H. (2007). Siberia, the wandering northern terrane, and its changing geography through the Palaeozoic. *Earth-Science Reviews*, 82(1–2), 29–74. <https://doi.org/10.1016/j.earscirev.2007.02.001>
- DeCelles, P. G., Ducea, M. N., Kapp, P., & Zandt, G. (2009). Cyclicity in Cordilleran orogenic systems. *Nature Geoscience*, 2(4), 251–257. <https://doi.org/10.1038/ngeo469>
- Deckart, K., Féraud, G., & Bertrand, H. (1997). Age of Jurassic continental tholeiites of French Guyana, Surinam and Guinea: Implications for the initial opening of the Central Atlantic Ocean. *Earth and Planetary Science Letters*, 150(3–4), 205–220. [https://doi.org/10.1016/S0012-821X\(97\)00102-7](https://doi.org/10.1016/S0012-821X(97)00102-7)
- Dergunov, A. B., Ryazantsev, A. V., Luneva, O. I., & Rikhter, A. V. (1997). Structure and geological history of the Bayan-Khongor Zone, central Mongolia. *Geotectonics*, 31, 132–140.
- Dijkstra, A. H., Brouwer, F. M., Cunningham, W. D., Buchan, C., Badarch, G., & Mason, P. R. (2006). Late Neoproterozoic proto-arc ocean crust in the Dariv Range, Western Mongolia: A supra-subduction zone end-member ophiolite. *Journal of the Geological Society*, 163(2), 363–373. <https://doi.org/10.1144/0016-764904-156>
- Donskaya, T. V., Gladkochub, D. P., Fedorovsky, V. S., Sklyarov, E. V., Cho, M., Sergeev, S. A., et al. (2017). Pre-collisional (>0.5 Ga) complexes of the Olkhon terrane (southern Siberia) as an echo of events in the Central Asian Orogenic Belt. *Gondwana Research*, 42, 243–263. <https://doi.org/10.1016/j.gr.2016.10.016>
- Donskaya, T. V., Gladkochub, D. P., Mazukabzov, A. M., Sklyarov, E. V., Khubanov, V. B., Demonterova, E. I., & Motova, Z. L. (2022). Metaterrigenous rocks of the Olkhon terrane of the Central Asian Orogenic Belt: U-Pb zircon age, geochemical characteristics, and formation models of sedimentary protoliths. *Geodynamics & Tectonophysics*, 13(3), 0635. <https://doi.org/10.5800/gt-2022-13-3-0635>
- Donskaya, T. V., Sklyarov, E. V., Gladkochub, D. P., Mazukabzov, A. M., Sal'nikova, E. B., Kovach, V. P., et al. (2000). The pribaikalian collisional metamorphic belt. *Doklady Akademii Nauk-Rossiyskaya Akademiya Nauk*, 374(1), 79–83.
- Ducea, M. (2001). The California arc: Thick granitic batholiths, eclogitic residues, lithospheric-scale thrusting, and magmatic flare-ups. *Geological Society of America Today*, 11(11), 4. [https://doi.org/10.1130/1052-5173\(2001\)011<0004:TCATGB>2.0.CO;2](https://doi.org/10.1130/1052-5173(2001)011<0004:TCATGB>2.0.CO;2)
- Ducea, M. N., Saleeby, J. B., & Bergantz, G. (2015). The architecture, chemistry, and evolution of continental magmatic arcs. *Annual Review of Earth and Planetary Sciences*, 43(1), 299–331. <https://doi.org/10.1146/annurev-earth-060614-105049>
- Dunne, G. C., & Walker, J. D. (2004). Structure and evolution of the East Sierran thrust system, east central California. *Tectonics*, 23(4). <https://doi.org/10.1029/2002TC001478>

- Fedorovsky, V. S., Sklyarov, E. V., Gladkochub, D. P., Mazukabzov, A. M., Donskaya, T. V., Lavrenchuk, A. V., et al. (2020). Collision system of west Pribaikalie: Aerospace geological map of Olkhon region (Baikal, Russia). *Geodynamics & Tectonophysics*, 11(3), 447–452. <https://doi.org/10.5800/GT-2020-11-3-0485>
- Fedorovsky, V. S., Sklyarov, E. V., Izokh, A. E., Kotov, A. B., Lavrenchuk, A. V., & Mazukabzov, A. M. (2010). Strike-slip tectonics and subalkaline mafic magmatism in the Early Paleozoic collisional system of the western Baikal region. *Russian Geology and Geophysics*, 51(5), 534–547. <https://doi.org/10.1016/j.rgg.2010.04.009>
- Gladkochub, D. P., Donskaya, T. V., Wingate, M. T., Poller, U., Kröner, A., Fedorovsky, V. S., et al. (2008). Petrology, geochronology, and tectonic implications of c. 500 Ma metamorphic and igneous rocks along the northern margin of the Central Asian Orogen (Olkhon terrane, Lake Baikal, Siberia). *Journal of the Geological Society*, 165(1), 235–246. <https://doi.org/10.1144/0016-76492006-125>
- Gordienko, I. V., Bulgatov, A. N., Ruzhentsev, S. V., Minina, O. R., Klimuk, V. S., Vetluzhskikh, L. I., et al. (2010). The Late Riphean–Paleozoic history of the Uda–Vitim island arc system in the Transbaikalian sector of the Paleozoic ocean. *Russian Geology and Geophysics*, 51(5), 461–481. <https://doi.org/10.1016/j.rgg.2010.04.005>
- Gordienko, I. V., Filimonov, A. V., Minina, O. R., Gornova, M. A., Medvedev, A. Y., Klimuk, V. S., et al. (2007). Dzhida island-arc system in the Paleozoic Ocean: Structure and main stages of Vendian–Paleozoic geodynamic evolution. *Russian Geology and Geophysics*, 48(1), 91–106. <https://doi.org/10.1016/j.rgg.2006.12.009>
- Gordienko, I. V., Kovach, V. P., Elbaev, A. L., Kotov, A. B., Sal'nikova, E. B., Reznitskii, L. Z., et al. (2012). Collisional granitoids of the Dzhida zone of the Central Asian fold belt, Southwestern Transbaikalia: Age and conditions of the formation. *Petrology*, 20(1), 40–58. <https://doi.org/10.1134/S086959111201002X>
- Grand'Homme, A., Janots, E., Seydoux-Guillaume, A. M., Guillaume, D., Bosse, V., & Magnin, V. (2016). Partial resetting of the U–Th–Pb systems in experimentally altered monazite: Nanoscale evidence of incomplete replacement. *Geology*, 44(6), 431–434. <https://doi.org/10.1130/G37770.1>
- Guo, X., Takasu, A., Liu, Y., & Li, W. (2014). Zn-rich spinel in association with quartz in the al-rich metapelites from the Mashan khondalite series, NE China. *Journal of Earth Sciences*, 25(2), 207–223. <https://doi.org/10.1007/s12583-014-0428-4>
- Guy, A., Schulmann, K., Clauer, N., Hasalova, P., Seltmann, R., Armstrong, R., et al. (2014). Late Paleozoic–Mesozoic tectonic evolution of the Trans-Altai and South Gobi Zones in southern Mongolia based on structural and geochronological data. *Gondwana Research*, 25(1), 309–337. <https://doi.org/10.1016/j.gr.2013.03.014>
- Hanžl, P., Uhrová, L., Hrdličková, K., Schulmann, K., Buriánek, D., Gansukh, O., & Míková, J. (2024). Late Ordovician magmatic pulse in the Tugrug Group, the Gobi Altai Zone, SW Mongolia. *Journal of Geosciences*, 69(1), 3–19. <https://doi.org/10.3190/jgeosci.385>
- Heister, T., Dannberg, J., Gassmüller, R., & Bangerth, W. (2017). High accuracy mantle convection simulation through modern numerical methods—II: Realistic models and problems. *Geophysical Journal International*, 210(2), 833–851. <https://doi.org/10.1093/gji/ggx195>
- Hippolyte, J. C., Angelier, J., & Barrier, E. (1995). Compressional and extensional tectonics in an arc system: Example of the Southern Apennines. *Journal of Structural Geology*, 17(12), 1725–1740. [https://doi.org/10.1016/0191-8141\(95\)00066-M](https://doi.org/10.1016/0191-8141(95)00066-M)
- Janoušek, V., Jiang, Y., Buriánek, D., Schulmann, K., Hanžl, P., Soejono, I., et al. (2018). Cambrian–ordovician magmatism of the Ikh-Mongol Arc system exemplified by the Khantaishir Magmatic Complex (Lake Zone, south-central Mongolia). *Gondwana Research*, 54, 122–149. <https://doi.org/10.1016/j.gr.2017.10.003>
- Jiang, J. S. (1992). Peak regional metamorphism of the khondalite series of the Mashan Group and its evolution. *Acta Petrologica et Mineralogica*, 11, 97–108.
- Jiang, Y., Sun, M., Zhao, G., Yuan, C., Xiao, W., Xia, X., et al. (2011). Precambrian detrital zircons in the Early Paleozoic Chinese Altai: Their provenance and implications for the crustal growth of central Asia. *Precambrian Research*, 189(1–2), 140–154. <https://doi.org/10.1016/j.precamres.2011.05.008>
- Jiang, Y. D., Schulmann, K., Kröner, A., Sun, M., Lexa, O., Janoušek, V., et al. (2017). Neoproterozoic–early Paleozoic peri-Pacific accretionary evolution of the Mongolian Collage system: Insights from geochemical and U–Pb zircon data from the Ordovician sedimentary wedge in the Mongolian Altai. *Tectonics*, 36(11), 2305–2331. <https://doi.org/10.1002/2017TC004533>
- Jiang, Y. D., Schulmann, K., Sun, M., Štípská, P., Guy, A., Janoušek, V., et al. (2016). Anatexis of accretionary wedge, Pacific-type magmatism, and formation of vertically stratified continental crust in the Altai Orogenic Belt. *Tectonics*, 35(12), 3095–3118. <https://doi.org/10.1002/2016TC004271>
- Jouvent, M., Peřestý, V., Jeřábek, P., Lexa, O., & Kylander-Clark, A. R. (2023). Assembly of the Variscan Orogenic Wedge in the Bohemian Massif: Monazite U–Pb geochronology of the tectonic events recorded in Saxothuringian metasediments. *Tectonics*, 42(4), e2022TC007626. <https://doi.org/10.1029/2022TC007626>
- Karmysheva, I. V., Vladimirov, V. G., Rudnev, S. N., Yakovlev, V. A., & Semenova, D. V. (2021). Syntectonic metamorphism of a collisional zone in the Tuva–Mongolian massif, Central Asian Orogenic belt: PT conditions, U–Pb ages and tectonic setting. *Journal of Asian Earth Sciences*, 220, 104919. <https://doi.org/10.1016/j.jseae.2021.104919>
- Karmysheva, I. V., Vladimirov, V. G., & Vladimirov, A. G. (2017). Synkinematic granitoid magmatism of western Sangilen, south-east Tuva. *Petrology*, 25(1), 87–113. <https://doi.org/10.1134/S0869591117010040>
- Kelly, N. M., Harley, S. L., & Möller, A. (2012). Complexity in the behavior and recrystallization of monazite during high-T metamorphism and fluid infiltration. *Chemical Geology*, 322, 192–208. <https://doi.org/10.1016/j.chemgeo.2012.07.001>
- Kovach, V., Kozakov, I., Kröner, A., Salnikova, E., Wang, K. L., Lee, H. Y., et al. (2021). Early Neoproterozoic crustal growth and microcontinent formation of the north–central Central Asian Orogenic Belt: New geological, geochronological, and Nd–Hf isotopic data on the Mélange Zone within the Zavkhan terrane, western Mongolia. *Gondwana Research*, 91, 254–276. <https://doi.org/10.1016/j.gr.2020.12.022>
- Kovach, V. P., Yarmolyuk, V. V., Kovalenko, V. I., Kozlovskiy, A. M., Kotov, A. B., & Terent'Eva, L. B. (2011). Composition, sources, and mechanisms of formation of the continental crust of the Lake Zone of the Central Asian Caledonides. II. Geochemical and Nd isotope data. *Petrology*, 19(4), 399–425. <https://doi.org/10.1134/S0869591111030064>
- Kozakov, I. K., Kotov, A. B., Sal'nikova, E. B., Kovach, V. P., Natman, A., Bibikova, E. V., et al. (2001). Timing of the structural evolution of metamorphic rocks in the Tuva–Mongolian Massif. *Geotectonics*, 35, 165–184.
- Kozakov, I. K., Kovach, V. P., Bibikova, E. V., Kirnozova, T. I., Lykhin, D. A., Plotkina, Y. V., et al. (2014). Late Riphean episode in the formation of crystalline rock complexes in the Dzabkhan microcontinent: Geological, geochronologic, and Nd isotopic–geochemical data. *Petrology*, 22(5), 480–506. <https://doi.org/10.1134/S086959111405004X>
- Kozakov, I. K., Salnikova, E. B., Anisimova, I. V., Azimov, P. Y., Kovach, V. P., Plotkina, Y. V., et al. (2019). Tectonic position of the late Neoproterozoic–early Paleozoic metamorphic belts within the Tuva–Mongolian terrane of the Central Asian Orogenic Belt. *Petrology*, 27(1), 43–58. <https://doi.org/10.1134/S086959111805003X>
- Kozakov, I. K., Sal'nikova, E. B., Kotov, A. B., Kovach, V. P., Bibikova, E. V., & Kirnozova, T. I. (1999). Polychronous evolution of the paleozoic granitoid magmatism in the Tuva–Mongolia Massif: U–Pb geochronological data. *Petrology*, 7(6), 592–601.

- Kozakov, I. K., Sal'nikova, E. B., Wang, T., Didenko, A. N., Plotkina, Y. V., & Podkovyrov, V. N. (2007). Early Precambrian crystalline complexes of the central Asian microcontinent: Age, sources, tectonic position. *Stratigraphy and Geological Correlation*, 15(2), 121–140. <https://doi.org/10.1134/S0869593807020013>
- Kronbichler, M., Heister, T., & Bangerth, W. (2012). High accuracy mantle convection simulation through modern numerical methods. *Geophysical Journal International*, 191(1), 12–29. <https://doi.org/10.1111/j.1365-246x.2012.05609.x>
- Kröner, A., Kovach, V., Belousova, E., Hegner, E., Armstrong, R., Dolgoplova, A., et al. (2014). Reassessment of continental growth during the accretionary history of the Central Asian Orogenic Belt. *Gondwana Research*, 25(1), 103–125. <https://doi.org/10.1016/j.gr.2012.12.023>
- Kröner, A., Lehmann, J., Schulmann, K., Demoux, A., Lexa, O., Tomurhuu, D., et al. (2010). Lithostratigraphic and geochronological constraints on the evolution of the Central Asian Orogenic Belt in SW Mongolia: Early Paleozoic rifting followed by late Paleozoic accretion. *American Journal of Science*, 310(7), 523–574. <https://doi.org/10.2475/07.2010.01>
- Levashova, N. M., Kalugin, V. M., Gibsher, A. S., Yff, J., Ryabinin, A. B., Meert, J. G., & Malone, S. J. (2010). The origin of the Baydaric microcontinent, Mongolia: Constraints from paleomagnetism and geochronology. *Tectonophysics*, 485(1–4), 306–320. <https://doi.org/10.1016/j.tecto.2010.01.012>
- Lexa, O. (2023). APSG, structural geology package for Python (version 1.2.1) [Software]. *Zenodo*. <https://doi.org/10.5281/zenodo.593586>
- Li, X. C., Yu, J. H., Sang, L. Q., Luo, L., & Zhu, G. R. (2009). Granulite facies metamorphism of the Olkhon terrane in southern Siberian Craton and tectonic significance. *Acta Petrologica Sinica*, 25, 3346–3356.
- Li, Z., Jiang, Y., Collett, S., Štípská, P., Schulmann, K., Wang, S., & Sukhorukov, V. (2023b). Metamorphic and chronological constraints on the early Paleozoic tectono-thermal evolution of the Olkhon Terrane, southern Siberia. *Journal of Metamorphic Geology*, 41(4), 525–556. <https://doi.org/10.1111/jmg.12706>
- Li, Z.-Y., Jiang, Y., Collett, S., Štípská, P., Schulmann, K., Wang, S., et al. (2023a). Peri-Siberian Ordovician to Devonian tectonic switching in the Olkhon Terrane (southern Siberia): Structural and geochronological constraints. *Tectonics*, 42(10), e2023TC007826. <https://doi.org/10.1029/2023TC007826>
- Liu, Y., Xiao, W., Ma, Y., Li, S., Peskov, A. Y., Chen, Z., et al. (2023). Oroclines in the Central Asian Orogenic Belt. *National Science Review*, 10(2), nwac243. <https://doi.org/10.1093/nsr/nwac243>
- Long, X., Sun, M., Yuan, C., Xiao, W., Lin, S., Wu, F., et al. (2007). Detrital zircon age and Hf isotopic studies for metasedimentary rocks from the Chinese Altai: Implications for the Early Paleozoic tectonic evolution of the Central Asian Orogenic Belt. *Tectonics*, 26(5). <https://doi.org/10.1029/2007TC002128>
- Lu, L. Z., Xu, X. C., & Liu, F. L. (1996). *The Precambrian khondalite series of northern China* (pp. 16–69). Changchun Publishing House.
- Makrygina, V. A., Tolmacheva, E. V., & Lepekhina, E. N. (2014). Crystallization history of Paleozoic granitoids in the Ol'khon region, Lake Baikal (SHRIMP-II zircon dating). *Russian Geology and Geophysics*, 55(1), 33–45. <https://doi.org/10.1016/j.rgg.2013.12.010>
- Malavieille, J. (2010). Impact of erosion, sedimentation, and structural heritage on the structure and kinematics of orogenic wedges: Analog models and case studies. *Geological Society of America Today*, 20(1), 4–10. <https://doi.org/10.1130/gsatg48a.1>
- Marinov, N. A., Zonenshain, L. P., & Blagonravov, V. A. (1973). *Geology of Mongolian Republic* (pp. 1–782). Nedra. (in Russian).
- Mikheev, E. I., Vladimirov, A. G., Fedorovsky, V. S., Bayanova, T. B., Mazukabov, A. M., Travin, A. V., et al. (2017). Age of overthrust-type granites in the accretionary-collisional system of the early Caledonides (western Baikal region). *Doklady Earth Sciences*, 472(2), 152–158. <https://doi.org/10.1134/s1028334x17020167>
- Mitrofanov, F. P., Bibikova, E. V., Gracheva, T. V., Kozakov, I. K., Sumin, L. V., & Shuleshko, I. K. (1985). Archaean isotope age of tonalite (“grey”) gneisses in Caledonian structure of Central Mongolia. *Doklady Akademii Nauk SSSR*, 284, 671–674. (in Russian).
- Mossakovsky, A., Ruzhentsev, S. V., Samygin, S. G., & Kheraskova, T. (1993). Central Asian fold belt: Geodynamic evolution and history of formation. *Geotectonics*, 6, 3–33.
- Motova, Z. L., Donskaya, T. V., Gladkochub, D. P., & Khubanov, V. B. (2024). U-Pb ages of detrital zircons and composition of clastic sedimentary rocks from the southern periphery of the Siberian craton: Implications for the earliest Cambrian evolution of southern Siberia. *Journal of Asian Earth Sciences*, 264, 106048. <https://doi.org/10.1016/j.jseae.2024.106048>
- Nozhkin, A. D., Bayanova, T. B., Turkina, O. M., Travin, A. V., & Dmitrieva, N. V. (2005). Early Paleozoic granitoid magmatism and metamorphism on the Derba microcontinent, eastern Sayan region: New isotope–geochronological data. *Doklady Earth Sciences*, 404, 1084–1089.
- Ota, T., Buslov, M. M., & Watanabe, T. (2002). Metamorphic evolution of Late Precambrian eclogites and associated metabasites, Gornyy Altai, southern Russia. *International Geology Review*, 44(9), 837–858. <https://doi.org/10.2747/0020-6814.44.9.837>
- Pefestý, V., Lexa, O., & Jiráček, P. (2020). Restoration of early-Variscan structures exposed along the Teplá shear zone in the Bohemian Massif: Constraints from kinematic modelling. *International Journal of Earth Sciences*, 109(4), 1189–1211. <https://doi.org/10.1007/s00531-019-01806-7>
- Ramsay, J. G. (1967). *Folding and fracturing of rocks* (p. 568). Mc Graw Hill Book Company.
- Riel, N., Kaus, B. J., Green, E. C. R., & Berlie, N. (2022). MAGEMin, an efficient Gibbs energy minimizer: Application to igneous systems. *Geochemistry, Geophysics, Geosystems*, 23(7), e2022GC010427. <https://doi.org/10.1029/2022GC010427>
- Rubatto, D., Chakraborty, S., & Dasgupta, S. (2013). Timescales of crustal melting in the Higher Himalayan Crystallines (Sikkim, Eastern Himalaya) inferred from trace element-constrained monazite and zircon chronology. *Contributions to Mineralogy and Petrology*, 165(2), 349–372. <https://doi.org/10.1007/s00410-012-0812-y>
- Rudnev, S. N., Izokh, A. E., Kovach, V. P., Shelepaev, R. A., & Terent'eva, L. B. (2009). Age, composition, sources, and geodynamic environments of the origin of granitoids in the northern part of the Ozernaya Zone, Western Mongolia: Growth mechanisms of the Paleozoic continental crust. *Petrology*, 17(5), 439–475. <https://doi.org/10.1134/S0869591109050026>
- Rudnev, S. N., Kovach, V. P., & Ponomarchuk, V. A. (2013). Vendian–Early Cambrian island-arc plagiogranitoid magmatism in the Altai–Sayan folded area and in the Lake Zone of western Mongolia (geochronological, geochemical, and isotope data). *Russian Geology and Geophysics*, 54(10), 1272–1287. <https://doi.org/10.1016/j.rgg.2013.09.010>
- Safonova, I., Kotlyarov, A., Krivonogov, S., & Xiao, W. (2017). Intra-oceanic arcs of the Paleo-Asian Ocean. *Gondwana Research*, 50, 167–194. <https://doi.org/10.1016/j.gr.2017.04.005>
- Salnikova, E. B., Kozakov, I. K., Kotov, A. B., Kröner, A., Todt, W., Bibikova, E. V., & Kovach, V. P. (2001). Age of Palaeozoic granites and metamorphism in the Tuvino-Mongolian Massif of the Central Asian Mobile Belt: Loss of a Precambrian microcontinent. *Precambrian Research*, 110(1–4), 143–164. [https://doi.org/10.1016/S0301-9268\(01\)00185-1](https://doi.org/10.1016/S0301-9268(01)00185-1)
- Schulz, B. (2021). Monazite microstructures and their interpretation in petrochronology. *Frontiers in Earth Science*, 9, 668566. <https://doi.org/10.3389/feart.2021.668566>
- Sengör, A. C., & Natal'in, B. A. (1996). Turkic-type orogeny and its role in the making of the continental crust. *Annual Review of Earth and Planetary Sciences*, 24(1), 263–337. <https://doi.org/10.1146/annurev.earth.24.1.263>

- Sengör, A. M. C., Natal'in, B. A., & Burtman, V. S. (1993). Evolution of the Altaid tectonic Collage and Palaeozoic crustal growth in Eurasia. *Nature*, 364(6435), 299–307. <https://doi.org/10.1038/364299a0>
- Sklyarov, E. V., Lavrenchuk, A. V., Fedorovsky, V. S., Gladkochub, D. P., Donskaya, T. V., Kotov, A. B., et al. (2020). Regional, contact metamorphism, and autometamorphism of the Olkhon Terrane (West Baikal Area). *Petrology*, 28(1), 47–61. <https://doi.org/10.1134/S0869591120010051>
- Skuzovatov, S. (2021). Nature and (in-) coherent metamorphic evolution of subducted continental crust in the Neoproterozoic accretionary collage of SW Mongolia. *Geoscience Frontiers*, 12(3), 101097. <https://doi.org/10.1016/j.gsf.2020.10.004>
- Skuzovatov, S. Y., Shatsky, V. S., Dril, S. I., & Perepelov, A. B. (2018). Elemental and isotopic (Nd-Sr-O) geochemistry of eclogites from the Zamtyin-Nuruu area (SW Mongolia): Crustal contribution and relation to Neoproterozoic subduction-accretion events. *Journal of Asian Earth Sciences*, 167, 33–51. <https://doi.org/10.1016/j.jseas.2017.11.032>
- Soejono, I., Burianek, D., Svojtka, M., Zacek, V., Cap, P., & Janousek, V. (2016). Mid-Ordovician and Late Devonian magmatism in the Togtokhinshil Complex: New insight into the formation and accretionary evolution of the Lake Zone (western Mongolia). *Journal of Geosciences*, 61(1), 5–23. <https://doi.org/10.3190/jgeosci.208>
- Soejono, I., Čáp, P., Míková, J., Janoušek, V., Buriánek, D., & Schulmann, K. (2018). Early Palaeozoic sedimentary record and provenance of flysch sequences in the Hovd Zone (western Mongolia): Implications for the geodynamic evolution of the Altai accretionary wedge system. *Gondwana Research*, 64, 163–183. <https://doi.org/10.1016/j.gr.2018.07.005>
- Soejono, I., Collett, S., Schulmann, K., Štípská, P., Míková, J., Peřestý, V., et al. (2025). Neoproterozoic paleogeography and displacement of the Mongolian blocks constrained by detrital zircon ages and Hf isotopic systematics (Zavkhan Block, W Mongolia). *Precambrian Research*, 417, 107657. <https://doi.org/10.1016/j.precamres.2024.107657>
- Soejono, I., Janoušek, V., Peřestý, V., Schulmann, K., Svojtka, M., Hanžl, P., et al. (2023). From Rodinian passive margin to peri-Siberian continental arc: Evidence from the multiphase Neoproterozoic–early Paleozoic magmatic record of the Zavkhan Block in the Mongolian Collage. *Gondwana Research*, 121, 344–367. <https://doi.org/10.1016/j.gr.2023.05.001>
- Soejono, I., Peřestý, V., Schulmann, K., Čopjaková, R., Svojtka, M., Štípská, P., et al. (2021). Structural, metamorphic and geochronological constraints on Palaeozoic multi-stage geodynamic evolution of the Altai accretionary wedge system (Hovd Zone, western Mongolia). *Lithos*, 396, 106204. <https://doi.org/10.1016/j.lithos.2021.106204>
- Štípská, P., Peřestý, V., Soejono, I., Schulmann, K., Kylander-Clark, R. A., Aguilar, C., et al. (2023). Anticlockwise metamorphic paths at ca. 890–790 Ma from the NE Baidrag block, Mongolia, indicate back-arc compression at the Rodinia periphery. *Geoscience Frontiers*, 14(2), 101520. <https://doi.org/10.1016/j.gsf.2022.101520>
- Štípská, P., Schulmann, K., Lehmann, J., Corsini, M., Lexa, O., & Tomurhuu, D. (2010). Early Cambrian eclogites in SW Mongolia: Evidence that the Palaeo-Asian Ocean suture extends further east than expected. *Journal of Metamorphic Geology*, 28(9), 915–933. <https://doi.org/10.1111/j.1525-1314.2010.00899.x>
- Štípská, P., Schulmann, K., Soejono, I., Peřestý, V., Kylander-Clark, R. A., Collett, S., et al. (2024). Supra-subduction thickening of a continental back-arc: Ediacaran–early Cambrian (Baikalian) metamorphism in the NE Baidrag block (Mongolian Collage). *Gondwana Research*, 135, 234–265. <https://doi.org/10.1016/j.gr.2024.08.007>
- Štípská, P., Závada, P., Collett, S., Kylander-Clark, A. R., Hacker, B. R., Tabaud, A. S., & Racek, M. (2020). Eocene migmatite formation and diachronous burial revealed by petrochronology in NW Himalaya, Zaskar. *Journal of Metamorphic Geology*, 38(6), 655–691. <https://doi.org/10.1111/jmg.12534>
- Sukhbaatar, T., Schulmann, K., Janoušek, V., Soejono, I., Lexa, O., Míková, J., et al. (2024). Magmatic and sedimentological arguments for an Ediacaran active margin in the Bayankhongor Zone in western Mongolia, Central Asian Orogenic Belt. *Gondwana Research*, 134, 385–409. <https://doi.org/10.1016/j.gr.2024.07.017>
- Togtokh, D., Baatarhuyag, A., Bayardalay, S., & Usna-Ekh, T. (1995). *Results of 1: 200 000 scale geological mapping in the Khovd and Gobi-Altay provinces* (p. 4861). Ulaanbaatar, Geologic Information Center Open-File Report. (In Mongolian).
- Townsend, K. J., Miller, C. F., D'Andrea, J. L., Ayers, J. C., Harrison, T. M., & Coath, C. D. (2001). Low temperature replacement of monazite in the Ireteba granite, Southern Nevada: Geochronological implications. *Chemical Geology*, 172(1–2), 95–112. [https://doi.org/10.1016/S0009-2541\(00\)00238-2](https://doi.org/10.1016/S0009-2541(00)00238-2)
- Travin, A. V., Yudin, D. S., Vladimirov, A. G., Khromykh, S. V., Volkova, N. I., Mekhonoshin, A. S., & Kolotilina, A. T. (2009). Thermo-chronology of the Chernorud granulite zone, Ol'khon Region, Western Baikal area. *Geochemistry International*, 47(11), 1107–1124. <https://doi.org/10.1134/S0016702909110068>
- Tremblay, A., Ruffet, G., & Lemarchand, J. (2020). Timing and duration of Archean orogenic gold deposits in the Bourlamaque pluton, Val d'Or mining camp, Abitibi, Canada. *Ore Geology Reviews*, 127, 103812. <https://doi.org/10.1016/j.oregeorev.2020.103812>
- Vermeesch, P. (2018). IsoplotR: A free and open toolbox for geochronology. *Geoscience Frontiers*, 9(5), 1479–1493. <https://doi.org/10.1016/j.gsf.2018.04.001>
- Vladimirov, A. G., Volkova, N. I., Mekhonoshin, A. S., Travin, A. V., Vladimirov, V. G., Khromykh, S. V., et al. (2011). The geodynamic model of formation of early Caledonides in the Olkhon region (west Pribaikalie). *Doklady Earth Sciences*, 436(2), 203–209. <https://doi.org/10.1134/S1028334X10901234>
- Volkova, N. I., & Sklyarov, E. V. (2007). High-pressure complexes of Central Asian Fold Belt: Geologic setting, geochemistry, and geodynamic implications. *Russian Geology and Geophysics*, 48(1), 83–90. <https://doi.org/10.1016/j.rgg.2006.12.008>
- Volkova, N. I., Stupakov, S. I., Tret'yakov, G. A., Simonov, V. A., Travin, A. V., & Yudin, D. S. (2005). Blueschists from the Uimon Zone as evidence for Ordovician accretionary-collisional events in Gorny Altai. *Russian Geology and Geophysics*, 46(4), 367–382.
- Wang, J. M., Rubatto, D., & Zhang, J. J. (2015). Timing of partial melting and cooling across the Greater Himalayan Crystalline Complex (Nyalam, Central Himalaya): In-sequence thrusting and its implications. *Journal of Petrology*, 56(9), 1677–1702. <https://doi.org/10.1093/ptrology/egv050>
- Wilde, S. A. (2015). Final amalgamation of the Central Asian Orogenic Belt in NE China: Paleo-Asian Ocean closure versus Paleo-Pacific plate subduction—A review of the evidence. *Tectonophysics*, 662, 345–362. <https://doi.org/10.1016/j.tecto.2015.05.006>
- Wilde, S. A., Zhang, X., & Wu, F. (2000). Extension of a newly identified 500 Ma metamorphic terrane in North East China: Further U–Pb SHRIMP dating of the Mashan Complex, Heilongjiang Province, China. *Tectonophysics*, 328(1–2), 115–130. [https://doi.org/10.1016/S0040-1951\(00\)00180-3](https://doi.org/10.1016/S0040-1951(00)00180-3)
- Wilhem, C., Windley, B. F., & Stampfli, G. M. (2012). The Altaids of central Asia: A tectonic and evolutionary innovative review. *Earth-Science Reviews*, 113(3–4), 303–341. <https://doi.org/10.1016/j.earscirev.2012.04.001>
- Willett, S. D. (1999). Orogeny and orography: The effects of erosion on the structure of mountain belts. *Journal of Geophysical Research*, 104(B12), 28957–28981. <https://doi.org/10.1029/1999JB900248>

- Windley, B. F., Alexeev, D., Xiao, W., Kröner, A., & Badarch, G. (2007). Tectonic models for accretion of the Central Asian Orogenic Belt. *Journal of the Geological Society*, 164(1), 31–47. <https://doi.org/10.1144/0016-76492006-022>
- Xiao, W., Windley, B. F., Badarch, G., Sun, S., Li, J. L., Qin, K., & Wang, Z. (2004). Palaeozoic accretionary and convergent tectonics of the southern Altaids: Implications for the growth of Central Asia. *Journal of the Geological Society*, 161(3), 339–342. <https://doi.org/10.1144/0016-764903-165>
- Xiao, W., Windley, B. F., Han, C., Liu, W., Wan, B., Zhang, J. E., et al. (2018). Late Paleozoic to early Triassic multiple roll-back and oroclinal bending of the Mongolia Collage in Central Asia. *Earth-Science Reviews*, 186, 94–128. <https://doi.org/10.1016/j.earscirev.2017.09.020>
- Xiao, W., Windley, B. F., Sun, S., Li, J., Huang, B., Han, C., et al. (2015). A tale of amalgamation of three Permo-Triassic Collage systems in Central Asia: Oroclines, sutures, and terminal accretion. *Annual Review of Earth and Planetary Sciences*, 43(1), 477–507. <https://doi.org/10.1146/annurev-earth-060614-105254>
- Xiao, W. J., Windley, B. F., Huang, B. C., Han, C. M., Yuan, C., Chen, H. L., et al. (2009). End-Permian to mid-Triassic termination of the accretionary processes of the southern Altaids: Implications for the geodynamic evolution, Phanerozoic continental growth, and metallogeny of Central Asia. *International Journal of Earth Sciences*, 98(6), 1189–1217. <https://doi.org/10.1007/s00531-008-0407-z>
- Yakubchuk, A. (2017). Evolution of the Central Asian Orogenic Supercollage since late Neoproterozoic revised again. *Gondwana Research*, 47, 372–398. <https://doi.org/10.1016/j.gr.2016.12.010>
- Yang, H., Xu, W., Sorokin, A. A., Ovchinnikov, R. O., & Ge, W. (2020). Geochronology and geochemistry of Neoproterozoic magmatism in the Bureya Block, Russian Far East: Petrogenesis and implications for Rodinia reconstruction. *Precambrian Research*, 342, 105676. <https://doi.org/10.1016/j.precamres.2020.105676>
- Yang, Y., Liang, C., Neubauer, F., Zheng, C., Zhou, J., & Xu, X. (2023). A review of Neoproterozoic to early Palaeozoic rocks of the Jiamusi–Khanka Massif, NE China: A rifted fragment from the Siberian Craton? *International Geology Review*, 65(8), 1289–1319. <https://doi.org/10.1080/00206814.2022.2084646>
- Yang, Y., Liang, C., Zheng, C., Xu, X., Zhou, J., Zhou, X., & Cao, C. (2021). Metamorphic evolution of high-grade granulite-facies rocks of the Mashan Complex, Liumao area, eastern Heilongjiang Province, China: Evidence from zircon U–Pb geochronology, geochemistry and phase equilibria modelling. *Precambrian Research*, 355, 106095. <https://doi.org/10.1016/j.precamres.2021.106095>
- Yang, Y., Liang, C., Zheng, C., Xu, X., Zhou, X., & Hu, P. (2022). The metamorphic characteristics of metapelites of the Mashan group in Mashan area, eastern Heilongjiang Province, China: Constraint on the crustal evolution of the Jiamusi massif. *Gondwana Research*, 102, 299–331. <https://doi.org/10.1016/j.gr.2020.10.004>
- Yang, Y., Zheng, C., Liang, C., Xu, X., Zhou, J., & Zhou, X. (2021). Mineral phase equilibria and zircon geochronology constraining the P–T–t path of granulite-facies metapelites of the Mashan Complex in the Shangshanyang area, Eastern Heilongjiang Province, China. *Precambrian Research*, 362, 106283. <https://doi.org/10.1016/j.precamres.2021.106283>
- Yarmolyuk, V. V., Kovach, V. P., Kovalenko, V. I., Salnikova, E. B., Kozlovskii, A. M., Kotov, A. B., et al. (2011). Composition, sources, and mechanism of continental crust growth in the Lake Zone of the Central Asian Caledonides: I. Geological and geochronological data. *Petrology*, 19(1), 55–78. <https://doi.org/10.1134/S0869591111010085>
- Zhou, J. B., Wang, B., Wilde, S. A., Zhao, G. C., Cao, J. L., Zheng, C. Q., & Zeng, W. S. (2015). Geochemistry and U–Pb zircon dating of the Toudaoqiao blueschists in the Great Xing'an Range, northeast China, and tectonic implications. *Journal of Asian Earth Sciences*, 97, 197–210. <https://doi.org/10.1016/j.jseaes.2014.07.011>
- Zhou, J. B., & Wilde, S. A. (2013). The crustal accretion history and tectonic evolution of the NE China segment of the Central Asian Orogenic Belt. *Gondwana Research*, 23(4), 1365–1377. <https://doi.org/10.1016/j.gr.2012.05.012>
- Zhou, J. B., Wilde, S. A., Zhang, X. Z., Ren, S. M., & Zheng, C. Q. (2011). Early Paleozoic metamorphic rocks of the Erguna block in the Great Xing'an Range, NE China: Evidence for the timing of magmatic and metamorphic events and their tectonic implications. *Tectonophysics*, 499(1–4), 105–117. <https://doi.org/10.1016/j.tecto.2010.12.009>
- Zhou, J. B., Wilde, S. A., Zhang, X. Z., Zhao, G. C., Liu, F. L., Qiao, D. W., et al. (2011). A >1300 km late Pan-African metamorphic belt in NE China: New evidence from the Xing'an block and its tectonic implications. *Tectonophysics*, 509(3–4), 280–292. <https://doi.org/10.1016/j.tecto.2011.06.018>
- Zhou, J. B., Wilde, S. A., Zhao, G. C., & Han, J. (2018). Nature and assembly of microcontinental blocks within the Paleo-Asian Ocean. *Earth-Science Reviews*, 186, 76–93. <https://doi.org/10.1016/j.earscirev.2017.01.012>
- Zhou, J. B., Wilde, S. A., Zhao, G. C., Zhang, X. Z., Zheng, C. Q., Wang, H. U., & Zeng, W. S. (2010). Pan-African metamorphic and magmatic rocks of the Khanka Massif, NE China: Further evidence regarding their affinity. *Geological Magazine*, 147(5), 737–749. <https://doi.org/10.1017/S0016756810000063>
- Zhu, M., Zhang, F., Smit, M. A., Pastor-Galán, D., Guilmette, C., Miao, L., et al. (2023). Discovery of a >1,000 km Cambrian eclogite-bearing high-pressure metamorphic belt in the Central Asian Orogenic Belt: Implications for the final closure of the Pan-Rodinnian Ocean. *Journal of Geophysical Research: Solid Earth*, 128(1), e2022JB025388. <https://doi.org/10.1029/2022JB025388>

References From the Supporting Information

- Aleinkoff, J. N., Schenck, W. S., Plank, M. O., Srogi, L., Fanning, C. M., Kamo, S. L., & Bosbyshell, H. (2006). Deciphering igneous and metamorphic events in high-grade rocks of the Wilmington Complex, Delaware: Morphology, cathodoluminescence and backscattered electron zoning, and SHRIMP U–Pb geochronology of zircon and monazite. *Geological Society of America Bulletin*, 118(1–2), 39–64. <https://doi.org/10.1130/B25659.1>
- Annen, C., Blundy, J. D., & Sparks, R. S. J. (2006). The genesis of intermediate and silicic magmas in deep crustal hot zones. *Journal of Petrology*, 47(3), 505–539. <https://doi.org/10.1093/petrology/egi084>
- Budzyń, B., Sláma, J., Corfu, F., Crowley, J., Schmitz, M., Williams, M. L., et al. (2021). TS-Mnz—a new monazite age reference material for U–Th–Pb microanalysis. *Chemical Geology*, 572, 120195. <https://doi.org/10.1016/j.chemgeo.2021.120195>
- Cao, W., Kaus, B. J., & Paterson, S. (2016). Intrusion of granitic magma into the continental crust facilitated by magma pulsing and dike-diapir interactions: Numerical simulations. *Tectonics*, 35(6), 1575–1594. <https://doi.org/10.1002/2015TC004076>
- Cheilletz, A., Ruffet, G., Marignac, C., Kolli, O., Gasquet, D., Féraud, G., & Bouillin, J. P. (1999). ⁴⁰Ar/³⁹Ar dating of shear zones in the Variscan basement of Greater Kabylia (Algeria). Evidence of an Eo-Alpine event at 128 Ma (Hauterivian–Barremian boundary): Geodynamic consequences. *Tectonophysics*, 306(1), 97–116. [https://doi.org/10.1016/S0040-1951\(99\)00047-5](https://doi.org/10.1016/S0040-1951(99)00047-5)
- Gonçalves, G. O., Lana, C., Scholz, R., Buick, I. S., Gerdes, A., Kamo, S. L., et al. (2016). An assessment of monazite from the Itambé pegmatite district for use as U–Pb isotope reference material for microanalysis and implications for the origin of the “Moacyr” monazite. *Chemical Geology*, 424, 30–50. <https://doi.org/10.1016/j.chemgeo.2015.12.019>

- De Putter, T., & Ruffet, G. (2020). Supergene manganese ore records 75 Myr-long Campanian to Pleistocene geodynamic evolution and weathering history of the Central African Great Lakes Region—Tectonics drives, climate assists. *Gondwana Research*, 83, 96–117. <https://doi.org/10.1016/j.gr.2020.01.021>
- De Putter, T., Ruffet, G., Yans, J., & Mees, F. (2015). The age of supergene manganese deposits in Katanga and its implications for the Neogene evolution of the African Great Lakes Region. *Ore Geology Reviews*, 71, 350–362. <https://doi.org/10.1016/j.oregeorev.2015.06.015>
- Fleck, R. J., Sutter, J. F., & Elliot, D. H. (1977). Interpretation of discordant $^{40}\text{Ar}/^{39}\text{Ar}$ age-spectra of Mesozoic tholeiites from Antarctica. *Geochimica et Cosmochimica Acta*, 41(1), 15–32. [https://doi.org/10.1016/0016-7037\(77\)90184-3](https://doi.org/10.1016/0016-7037(77)90184-3)
- Fletcher, I. R., McNaughton, N. J., Aleinikoff, J. A., Rasmussen, B., & Kamo, S. L. (2004). Improved calibration procedures and new standards for U–Pb and Th–Pb dating of Phanerozoic xenotime by ion microprobe. *Chemical Geology*, 209(3–4), 295–314. <https://doi.org/10.1016/j.chemgeo.2004.06.015>
- Holland, T. J. B., & Powell, R. (2011). An improved and extended internally consistent thermodynamic dataset for phases of petrological interest, involving a new equation of state for solids. *Journal of Metamorphic Geology*, 29(3), 333–383. <https://doi.org/10.1111/j.1525-1314.2010.00923.x>
- Holland, T. J. B., Green, E. C. R., & Powell, R. (2022). A thermodynamic model for feldspars in KAlSi_3O_8 – $\text{NaAlSi}_3\text{O}_8$ – $\text{CaAl}_2\text{Si}_2\text{O}_8$ for mineral equilibrium calculations. *Journal of Metamorphic Geology*, 40(4), 587–600. <https://doi.org/10.1111/jmg.12639>
- Horstwood, M. S., Foster, G. L., Parrish, R. R., Noble, S. R., & Nowell, G. M. (2003). Common-Pb corrected in situ U–Pb accessory mineral geochronology by LA-MC-ICP-MS. *Journal of Analytical Atomic Spectrometry*, 18(8), 837–846. <https://doi.org/10.1039/B304365G>
- Horstwood, M. S., Košler, J., Gehrels, G., Jackson, S. E., McLean, N. M., Paton, C., et al. (2016). Community-derived standards for LA-ICP-MS U–(Th)–Pb geochronology—Uncertainty propagation, age interpretation and data reporting. *Geostandards and Geoanalytical Research*, 40(3), 311–332. <https://doi.org/10.1111/j.1751-908X.2016.00379.x>
- Hyndman, R. D. (2019). Origin of regional Barrovian metamorphism in hot backarcs prior to orogeny deformation. *Geochemistry, Geophysics, Geosystems*, 20(1), 460–469. <https://doi.org/10.1029/2018GC007650>
- Jourdan, F., & Renne, P. R. (2007). Age calibration of the Fish Canyon sanidine $^{40}\text{Ar}/^{39}\text{Ar}$ dating standard using primary K–Ar standards. *Geochimica et Cosmochimica Acta*, 71(2), 387–402. <https://doi.org/10.1016/j.gca.2006.09.002>
- Jourdan, F., Verati, C., & Féraud, G. (2006). Intercalibration of the Hb3gr $^{40}\text{Ar}/^{39}\text{Ar}$ dating standard. *Chemical Geology*, 231(3), 177–189. <https://doi.org/10.1016/j.chemgeo.2006.01.027>
- Kretz, R. (1983). Symbols for rock-forming minerals. *American Mineralogist*, 68(1–2), 277–279.
- Kylander-Clark, A. R., Hacker, B. R., & Cottle, J. M. (2013). Laser-ablation split-stream ICP petrochronology. *Chemical Geology*, 345, 99–112. <https://doi.org/10.1016/j.chemgeo.2013.02.019>
- Malo, M., Ruffet, G., Pinciv, A., & Tremblay, A. (2008). A $^{40}\text{Ar}/^{39}\text{Ar}$ study of oceanic and continental deformation processes during an oblique collision: Taconian orogeny in the Quebec reentrant of the Canadian Appalachians. *Tectonics*, 27(4). <https://doi.org/10.1029/2006TC002094>
- Nteme, J., Scaillet, S., Brault, P., & Tassan-Got, L. (2022). Atomistic simulations of ^{40}Ar diffusion in muscovite. *Geochimica et Cosmochimica Acta*, 331, 123–142. <https://doi.org/10.1016/j.gca.2022.05.004>
- Palin, R. M., Searle, M. P., Waters, D. J., Parrish, R. R., Roberts, N. M. W., Horstwood, M. S. A., et al. (2013). A geochronological and petrological study of anatectic paragneiss and associated granite dykes from the Day Nui Con Voi metamorphic core complex, North Vietnam: Constraints on the timing of metamorphism within the Red River shear zone. *Journal of Metamorphic Geology*, 31(4), 359–387. <https://doi.org/10.1111/jmg.12025>
- Paton, C., Woodhead, J. D., Hellstrom, J. C., Hergt, J. M., Greig, A., & Maas, R. (2010). Improved laser ablation U–Pb zircon geochronology through robust downhole fractionation correction. *Geochemistry, Geophysics, Geosystems*, 11(3). <https://doi.org/10.1029/2009GC002618>
- Paton, C., Hellstrom, J., Paul, B., Woodhead, J., & Hergt, J. (2011). Lolite: Freeware for the visualisation and processing of mass spectrometric data. *Journal of Analytical Atomic Spectrometry*, 26(12), 2508–2518. <https://doi.org/10.1039/c1ja10172b>
- Perrot, M., Tremblay, A., Ruffet, G., Labrousse, L., Gervais, F., & Caroir, F. (2020). Diachronic metamorphic and structural evolution of the Connecticut Valley–Gaspé trough, Northern Appalachians. *Journal of Metamorphic Geology*, 38(1), 3–27. <https://doi.org/10.1111/jmg.12510>
- Petrus, J. A., & Kamber, B. S. (2012). VizualAge: A novel approach to laser ablation ICP-MS U–Pb geochronology data reduction. *Geostandards and Geoanalytical Research*, 36(3), 247–270. <https://doi.org/10.1111/j.1751-908X.2012.00158.x>
- Rees Jones, D. W., Katz, R. F., Tian, M., & Rudge, J. F. (2018). Thermal impact of magmatism in subduction zones. *Earth and Planetary Science Letters*, 481, 73–79. <https://doi.org/10.1016/j.epsl.2017.10.015>
- Renne, P. R., Mundil, R., Balco, G., Min, K., & Ludwig, K. R. (2010). Joint determination of ^{40}K decay constants and $^{40}\text{Ar}/^{40}\text{K}$ for the Fish Canyon sanidine standard, and improved accuracy for $^{40}\text{Ar}/^{39}\text{Ar}$ geochronology. *Geochimica et Cosmochimica Acta*, 74(18), 5349–5367. <https://doi.org/10.1016/j.gca.2010.06.017>
- Renne, P. R., Balco, G., Ludwig, K. R., Mundil, R., & Min, K. (2011). Response to the comment by WH Schwarz et al. on “Joint determination of ^{40}K decay constants and $^{40}\text{Ar}/^{40}\text{K}$ for the Fish Canyon sanidine standard, and improved accuracy for $^{40}\text{Ar}/^{39}\text{Ar}$ geochronology” by PR Renne et al. (2010). *Geochimica et Cosmochimica Acta*, 75(17), 5097–5100. <https://doi.org/10.1016/j.gca.2011.06.021>
- Roddick, J. C. (1983). High precision intercalibration of ^{40}Ar – ^{39}Ar standards. *Geochimica et Cosmochimica Acta*, 47(5), 887–898. [https://doi.org/10.1016/0016-7037\(83\)90154-0](https://doi.org/10.1016/0016-7037(83)90154-0)
- Rothstein, D. A., & Manning, C. E. (2003). *Geothermal gradients in continental magmatic arcs: Constraints from the eastern Peninsular Ranges batholith, Baja California, México* (pp. 337–354). Special Papers–Geological Society of America. <https://doi.org/10.1130/0-8137-2374-4.337>
- Ruffet, G., Féraud, G., & Amouric, M. (1991). Comparison of ^{40}Ar – ^{39}Ar conventional and laser dating of biotites from the North Trégor Batholith. *Geochimica et Cosmochimica Acta*, 55(6), 1675–1688. [https://doi.org/10.1016/0016-7037\(91\)90138-U](https://doi.org/10.1016/0016-7037(91)90138-U)
- Ruffet, G., Féraud, G., Balèvre, M., & Kiéna, J. R. (1995). Plateau ages and excess argon in phengites: An ^{40}Ar – ^{39}Ar laser probe study of Alpine micas (Sesia Zone, Western Alps, northern Italy). *Chemical Geology*, 121(1–4), 327–343. [https://doi.org/10.1016/0009-2541\(94\)00132-R](https://doi.org/10.1016/0009-2541(94)00132-R)
- Stacey, J. T., & Kramers, J. D. (1975). Approximation of terrestrial lead isotope evolution by a two-stage model. *Earth and Planetary Science Letters*, 26(2), 207–221. [https://doi.org/10.1016/0012-821X\(75\)90088-6](https://doi.org/10.1016/0012-821X(75)90088-6)
- Tajčmanová, L., Soejono, I., Konopásek, J., Košler, J., & Klötzli, U. (2010). Structural position of high-pressure felsic to intermediate granulites from NE Moldanubian domain (Bohemian Massif). *Journal of the Geological Society*, 167(2), 329–345. <https://doi.org/10.1144/0016-76492009-086>
- Tomaschak, P. B., Krogstad, E. J., & Walker, R. J. (1996). U–Pb monazite geochronology of granitic rocks from Maine: Implications for late Paleozoic tectonics in the Northern Appalachians. *The Journal of Geology*, 104(2), 185–195. <https://doi.org/10.1086/629813>
- Tunheng, A., & Hirata, T. (2004). Development of signal smoothing device for precise elemental analysis using laser ablation-ICP-mass spectrometry. *Journal of Analytical Atomic Spectrometry*, 19(7), 932–934. <https://doi.org/10.1039/B402493A>
- Turner, G., Huneke, J. C., Podosek, F. A., & Wasserburg, G. J. (1971). ^{40}Ar – ^{39}Ar ages and cosmic ray exposure ages of Apollo 14 samples. *Earth and Planetary Science Letters*, 12(1), 19–35. [https://doi.org/10.1016/0012-821X\(71\)90051-3](https://doi.org/10.1016/0012-821X(71)90051-3)

- White, R. W., Powell, R. O. G. E. R., Holland, T. J. B., Johnson, T. E., & Green, E. C. R. (2014a). New mineral activity–composition relations for thermodynamic calculations in metapelitic systems. *Journal of Metamorphic Geology*, 32(3), 261–286. <https://doi.org/10.1111/jmg.12071>
- White, R. W., Powell, R., & Johnson, T. E. (2014b). The effect of Mn on mineral stability in metapelites revisited: New a–x relations for manganese-bearing minerals. *Journal of Metamorphic Geology*, 32(8), 809–828. <https://doi.org/10.1111/jmg.12095>
- Wijbrans, J. R., & McDougall, I. (1986). $^{40}\text{Ar}/^{39}\text{Ar}$ dating of white micas from an Alpine high-pressure metamorphic belt on Naxos (Greece): The resetting of the argon isotopic system. *Contributions to Mineralogy and Petrology*, 93(2), 187–194. <https://doi.org/10.1007/BF00371320>